Manuscript
Click here to access/download;Manuscript;Main text - clean.docx
This is the Pre-Published Version.
This material may be downloaded for personal use only. Any other use requires prior permission of the American Society of Civil Engineers.
This material may be found at https://ascelibrary.org/doi/10.1061/JGGEFK.GTENG-12729.

Effects of curing temperature and stress on small strain stiffness of cemented marine clay

Authors: Kang-fu Jiao[1], Chao Zhou*[2], Wen-bo Chen[3] and Zhi-jian Ruan[4]

*Corresponding author

Information of the authors

[1] Ph.D. Student, Department of Civil and Environmental Engineering, The Hong Kong Polytechnic University, Hung Hom, Kowloon, Hong Kong.

Email: kangfu.jiao@connect.polyu.hk

[2] Tsui Tack Kong Young Scholar in Civil Engineering, Associate Professor, Department of Civil and Environmental Engineering, Research Institute for Sustainable Urban Development, The Hong Kong Polytechnic University, Hung Hom, Hong Kong.

Email: c.zhou@polyu.edu.hk

[3] Professor, College of Civil and Transportation Engineering, Shenzhen University, Nanshan District, Shenzhen 518060, China.

Email: wenbochen@szu.edu.cn

[4] Ph.D. Student. Department of Civil and Environmental Engineering, The Hong Kong Polytechnic University, Hung Hom, Kowloon, Hong Kong.

Email: james.ruan@connect.polyu.hk

Abstract

The deep cement mixing (DCM) method is widely used for ground improvement, with soils within DCM columns often subjected to varying curing temperatures (T_c) and curing stresses (S_c). Their effects on shear stiffness at small strains (0.001% to 1%), crucial for analyzing the serviceability limit state of DCM columns, have not been studied. In this study, a temperature and stress-controlled curing apparatus was newly developed and used to prepare cemented marine clay at three T_c (20, 30, and 40°C) and three S_c levels (0, 150, and 300 kPa). After 28 days of curing, unconfined compression tests with local strain measurements were conducted. Thermogravimetric (TG) analysis, scanning electron microscopy (SEM), and mercury intrusion porosimetry (MIP) tests were performed to analyze the composition and microstructure of cemented marine clay. Test results reveal that an increase in T_c and S_c can improve strength and stiffness, decrease the elastic threshold strain, and increase the rate of stiffness degradation within the small strain range. These findings are attributed to the fact that higher T_c can accelerate the cement hydration reaction, enhance the pozzolanic reaction, and alter the pore size distribution. While S_c has minimal impact on cement hydration, it leads to more effective cementitious bonding. The findings suggest that taking into account the effects of T_c and S_c can lead to more cost-effective designs. Based on the test results, a nonlinear equation was proposed to enhance the accuracy of calculating the secant Young's modulus, an important parameter in the DCM designs.

Keywords: cemented clay, curing temperature, curing stress, small strain stiffness

Introduction

DCM method has garnered great interest in recent decades. It is widely used in land reclamation for its short construction period and environmental sustainability (Cheung et al. 2022; Yin et al. 2022; Yin et al. 2023). Many studies have investigated the properties of cemented soils, such as their strength and stiffness. Most of these studies cured specimens at room temperature (usually 20-25°C) and without external loading. However, during in-site curing, DCM columns are subjected to various temperatures and stresses. According to the field data from Japan (Van Nguyen et al. 2021) and Norway (Bache et al. 2022), the temperature inside DCM columns can reach 40℃ due to cement hydration and last for a month. Furthermore, the length of DCM columns typically exceeds 10 meters, and the effective confining pressure from surrounding soils can vary widely, ranging from 0 to approximately 200-300 kPa (El Kamash et al. 2014; Jamsawang et al. 2016; Phutthananon et al. 2023; Zhao et al. 2023). Ignoring the distinctions between laboratory and field curing conditions may result in inaccurate parameters and improper designs. Therefore, it is crucial to investigate the impact of curing temperature and stress on the properties of cemented soils.

Furthermore, the performance of geostructures in DCM-stabilised ground at working conditions, such as retaining walls and tunnels, is greatly affected by ground movement. According to data from field monitoring, the typical strains encountered in DCM columns (Bergado and Lorenzo 2005; Liu et al. 2012; Melentijevic et al. 2013; Pongsivasathit et al. 2021) are generally in the small strain range (0.001% to 1%) at working conditions. A good understanding of cemented soil behaviour at small strains (Ng et al., 2024) is thus essential for analyzing the serviceability limit state of geostructures in DCM-stabilized ground.

So far, as far as the authors are aware, no research has studied the effect of curing temperature on the stiffness degradation of cemented soil within small strains. The effects of curing stress on stiffness within small strains have been studied by only a few studies and

have not been fully understood due to limited data. Consoli et al. (2000) and Marques et al. (2021) explored the effects of curing stress on the small strain stiffness of cemented sand using an external linear variable differential transformer (LVDT). Due to the low accuracy of external LVDTs, data in the strain range of less than 0.01% were not captured. Subramaniam and Banerjee (2020) investigated the influence of curing stress on the shear modulus degradation of cemented marine clay through resonant column tests. They found that at a confining pressure of 100 kPa, the shear modulus degradation rate was faster with a curing stress of 90 kPa compared to curing stresses of 30 and 60 kPa. However, the effects of curing stress were negligible at higher confining pressures (200 and 300 kPa). Therefore, more research is required to fully understand the influence of curing temperature and stress on the strain-dependent stiffness of cemented clay, particularly at small strains.

The objectives of this study are to investigate the effects of curing temperature and curing stress and their coupling effects on the behaviour of cemented marine clay, focusing on the small strain stiffness. A comprehensive experimental programme for curing and testing the specimens was designed. In addition, the mechanism of curing temperature and stress effect was explained by conducting microscopic experiments, including SEM test, MIP test, and TG analysis. Based on the new data, a new and simple method was proposed to improve the accuracy of the E_{50} calculation, which is the secant modulus at 50% of the unconfined compressive strength (UCS). Detailed information on the experimental setup, specimen preparation and testing, and result analysis are given below.

Materials and methods

Test programme

A comprehensive experimental program was designed and is summarized in Table 1, taking into account the effects of three factors: curing temperature, curing stress, and cement content. As aforementioned, the temperature inside DCM columns can reach 40°C due to

cement hydration. Therefore, this study selected three curing temperatures (i.e., 20, 30, and 40°C) ranging from room temperature to 40°C. The effective confining pressure from surrounding soils to DCM can reach several hundred kPa, depending on several factors, such as the DCM length, the unit weight, and the lateral stress coefficient of surrounding soils. The maximum stress in a typical DCM is approximately 200-300 kPa (El Kamash et al. 2014; Jamsawang et al. 2016; Phutthananon et al. 2023; Zhao et al. 2023), so three curing stress levels (i.e., 0, 150, and 300 kPa) were selected for the planned tests. The detailed test program is summarized in Table 1. Cement content (*Cc*) in Table 1 refers to the mass ratio of cement powder to dry soil.

Test materials

The binder used is Type I Ordinary Portland Cement (OPC), and its chemical composition is summarized in Table 2. The marine clay was sampled from Lamma Island, Hong Kong. To ensure that the largest particle size is less than one-fifth of the specimen diameter (50 mm in this study), particles larger than 5 mm in diameter were removed using wet sieving without a dispersant, following the Geospec 3 (2001) guidelines. The physical properties of the marine clay are summarized in Table 3, and the particle size distribution curve is shown in Figure 1. According to the Unified Soil Classification System of ASTM (2020) standard D2487, it is classified as a fat clay (CH). In addition, the loss on ignition (LOI) value for the marine clay is 4.31%, classifying it as a mineral soil with a certain amount of organic matter (Huang et al., 2008).

It has been well-recognized that clay content can affect the cementation effects. For example, Woo (1971) found that an increase in clay content and plasticity index would reduce the bonding effects. Subramanian et al. (2020) demonstrated that the ratio of compressional wave to shear wave increases with the increase in clay content for cemented soils. The current study does not specifically investigate the effects of clay content on

cemented marine clay, and the tested marine clay is found to have a clay content of 22%.

Specimen preparation

The specimen preparation involves five major steps, including clay slurry preparation, cement slurry preparation, soil-cement mixing, specimen moulding and curing. The total time required for specimen preparation is approximately 30 minutes, which is shorter than the initial setting time of Type I OPC (45 minutes). The specimen preparation details are as follows:

1. A specific amount of sieved marine clay was taken from a sealed container after being mixed with a portable mixer. The initial water content was controlled at 65%, with reference to the typical in-situ water contents of the tested marine clay.
2. The required amounts of cement powder and water were weighed and mixed in a 1:1 mass ratio to form a cement slurry (Wang et al., 2019), as shown in Figure 2a.
3. A mixer was used to blend the marine clay and cement (see Figure 2b) at low speed (e.g., 135 RPM) for 2 minutes and then at high speed (e.g., 220 RPM) for 3 minutes, refer to the procedure outlined in GEO (2023). The mixer was stopped for 60 seconds, and a spatula was used to scrape the mixture from the sides of the mixing bowl and the mixer attachment, pushing it back to the center of the bowl. Mixing continues at high speed (e.g., 220 RPM) for 5 minutes.
4. Once thoroughly mixed, the marine clay-cement mixture was immediately placed into moulds lubricated with petroleum jelly. Each mould was filled in three layers of approximately equal thickness. A vibrating table (60 Hz) was used to eliminate air bubbles, following the methods in ASTM (2013) standard C192.
5. The mould containing the cement-soil mixture was set up in a curing apparatus, as shown in Figure 2d. This curing apparatus was newly developed in this study, and its details are shown in Figure 3. It is able to control the curing temperature and stress.

To maintain temperature stability during the curing process, a temperature-controlled water bath was employed. A heater was installed at the bottom of the water bath, and its heating rate was regulated based on the reading of a thermocouple with an accuracy of 0.1°C, which was positioned at the mid-height of the water bath. In addition, to ensure uniform temperature distribution within the water tank, a water turbine was used to keep the water in motion. When the temperature reached equilibrium, the two thermocouples at different positions showed almost identical measurements and fluctuated by less than 0.1°C. On the other hand, the vertical curing stress was applied using pneumatic cylinders. The air pressure inside each pneumatic cylinder was maintained constant throughout the curing process to ensure the desired curing stress. Before specimen curing, the friction of the cylinder telescopic rod was measured using a load cell. The results showed that the friction of the cylinder was negligible (less than 5 N).

Unconfined compression tests

After 28 days of curing, the specimen underwent checks for flatness, perpendicularity, and parallelism before unconfined compression tests. The unconfined compression (UC) tests were conducted using the TRI-SCAN 100 device. The loading rate was set to 0.2 mm/min, consistent with the rate used by Ribeiro et al. (2016) and Cardoso et al. (2017) in their unconfined compression tests on cemented soil. The vertical strain of specimens was measured using a combination of strain gauges and local and global LVDTs, as depicted in Figure 4. The working range of the sensors is divided into 3 intervals: 0.001% - 0.1% (strain gauge with a strain accuracy of 0.0001%), 0.1% - 1% (local LVDT with a strain accuracy of 0.01%), and > 1% (global LVDT with a strain accuracy of 0.1%).

Microstructural analysis

To prepare specimens for the TG analysis, cemented specimens were frozen by

immersion in liquid nitrogen (-195°C) for 5 minutes. Subsequently, the frozen specimens were freeze-dried (− 85°C, 0.133 mbar) in a freeze-drier (Labconco Freezone 2.5 Plus) for 48 hours. Some freeze-dried specimens were then ground into fine powder (about 10 mg) for TG analysis (Netzsch STA 449F3). The testing temperature was increased from 30 to 1000°C with a heating rate of 10°C/min. During the heating process, nitrogen gas at a flow rate of 50 mL/min was used to prevent carbonation of the samples. Further details of the test method can be found in Scrivener et al. (2018).

The specimens for SEM and MIP tests were prepared using a method similar to that of the TG analysis, with one major difference. In contrast to the specimen preparation for TG analysis, the specimen preparation procedures for SEM and MIP testing require the exchange of water with ethanol (immersed in ethanol for 3 days) before freezing in liquid nitrogen, following the method of Han et al. (2014). The main purpose of this step was to prevent the volume expansion of pore water during liquid nitrogen freezing from damaging the cementation structure. After the liquid nitrogen treatment, the parallel specimens were freeze-dried in the freeze-drier. The morphologies were analyzed using an SEM (TESCAN VEGA 3) to investigate the micro-topography of cemented specimens. The pore size distribution was determined through MIP (Micromeritics Autopore V 9600) tests. In the analysis of MIP test data, a contact angle of 140° and a surface tension of mercury of 0.480 N/m were used.

Repeatability of the test results

In addition to the tests in Table 1, some additional tests were conducted to assess the repeatability of the results. In certain test conditions, two tests were conducted, as outlined in Table 4. The comparison between the two test results is shown in Figure 5. When the curing stress is zero, the largest difference between the two specimens is around 0.4 MPa, with a percentage difference of around 30%. This discrepancy may be attributed to the inhomogeneous distribution of cement particles. In contrast, when the curing stress is 150 and

300 kPa, the percentage difference between the specimens is less than 5% due to the increased uniformity resulting from the application of curing stress. These results suggest a generally good level of repeatability in the test results.

Results and discussion

Cemented marine clay with different cement contents

Figure 6a shows the stress-strain relationship of cemented marine clay with varying cement contents obtained from unconfined compression tests. As anticipated, the UCS increases with an increase in cement content, attributed to the growing cementation bonds as the cement content rises. The specimens demonstrate a brittle failure mode after reaching the peak strength, occurring at a strain of approximately 1.5%, due to the inherent brittleness of the cementitious matrix (Ismail et al., 2002).

Figure 6b illustrates the corresponding stiffness degradation curves. The secant Young's modulus is defined as the ratio of vertical stress to vertical strain. It was observed that specimens with higher cement content exhibit a higher modulus during compression. Moreover, an important parameter of the stiffness degradation curve is the elastic threshold strain (ε_e), which represents the point below which soil behaviour is predominantly elastic with an almost constant modulus, and the internal structure of the soil remains almost unchanged. In this study, ε_e was determined as the axial strain corresponding to E_{sec}/E_0 = 0.95, following the method used by Clayton and Heymann (2001). The obtained ε_e value is around 0.01%, and it slightly increased with an increase in cement content.

To gain a better understanding of the macro behaviour of cemented marine clay, Figure 7 shows SEM images of uncemented and cemented marine clay. At a magnification of 1000x (Figure 7a), the marine clay exhibits a microstructure with exposed inter-aggregate pores. Figures 7b and 7c are SEM images of uncemented marine clay at magnifications of 5000x and 8000x, respectively, showing widely distributed clay/silt aggregates in the specimens.

Figure 7d displays the SEM results of cemented marine clay at a magnification of 1000x, where the inter-aggregate pores are filled with cement hydration products. In comparison to the SEM image of uncemented marine clay, the structure of cemented marine clay appears more compacted, and the inter-aggregate pore size is significantly reduced. Figures 7e and 7f show SEM results of cemented soil after magnifications of 5000x and 8000x, revealing that the clay particles and silt grains are covered with reticulated morphology (Calcium silicate hydrate) and prismatic crystals (ettringite).

Influence of curing temperature on the mechanical behaviour of cemented marine clay

Figure 8 illustrates the UCS and E_{50} of specimens at different curing temperatures. As the curing temperature increased from 20 to 40°C, the UCS nearly doubled, and the E_{50} increased by approximately 50%. The increase in strength and stiffness with rising curing temperature can be attributed to the accelerated rate of cement hydration at elevated temperatures, leading to the production of more hydration products. Furthermore, higher temperatures promote pozzolanic reactions, which generate additional strength-enhancing hydration products. These hydration products fill the pores, effectively linking soil particles and aggregates, thereby increasing the contact stiffness and contact area between the soil particles. Consequently, both the strength and modulus were significantly improved. These observations are further elucidated later based on the results of TG analysis and MIP tests.

Figure 9 depicts the degradation curves of secant Young's modulus within a small strain range. When the axial strain is below approximately 0.01%, the soil behaviour is essentially elastic, and the shear stiffness remains almost constant at each curing temperature. However, when the strain exceeds 0.01%, the modulus degrades rapidly with increasing axial strain. Specimens cured at higher temperatures consistently exhibit a higher secant modulus, regardless of the strain amplitude.

To examine the potential influence of curing temperature on the stiffness degradation rate, the

246 secant Young's modulus E is normalized by E_0. Figure 10 shows the degradation curve of
247 E/E_0, with the results from the specimens with 15% cement content as an example. The
248 change in curing temperature slightly affects the degradation curve. Firstly, the elastic
249 threshold strain decreases with increasing curing temperature. Secondly, the degradation
250 curves for different curing temperatures intersect within the small strain range. Compared
251 with specimens cured at a lower temperature, the stiffness degradation rate for specimens
252 cured at a higher temperature is initially larger and subsequently becomes smaller (see Fig. 7).
253 This difference in stiffness degradation rates may be due to the fact that the stiffness
254 degradation is affected by different mechanisms. When the strain is relatively small, the
255 primary cause of stiffness degradation is the breakage of inter-particle bonds. Specimens
256 cured at higher temperatures have more cementation bonds, a more uniform pore size
257 distribution, and fewer large pores, as confirmed by the TG analysis and MIP test results
258 presented later. Consequently, as the strain increases, the cementation structure of these
259 specimens is easier to damage, resulting in a smaller elastic threshold and higher degradation
260 rate when the strain is relatively small. When the strain is relatively large, the rearrangement
261 of soil particles becomes the major reason for the stiffness degradation. As explained before,
262 the stiffness degradation induced by particle rearrangement is comparable, so the normalized
263 stiffness degradation rate with large E_0 is smaller.

264 To further analyze the stiffness degradation characteristics of uncemented marine clay,
265 predictions by the equation of Vardanega and Bolton (2013) are incorporated in Figure 10 for
266 comparison. Vardanega and Bolton (2013) summarized the shear modulus-strain response
267 data of 21 uncemented fine-grained soils, including clay and silt, and proposed a hyperbolic
268 model to model the shear modulus degradation curve of fine-grained soils. Their study
269 demonstrated that using the plasticity index (PI) of uncemented fine-grained soil as a model
270 parameter yields sufficiently accurate predictions of shear modulus degradation. Assuming

the degradation of shear modulus aligns with the degradation of Young's modulus, the degradation of Young's modulus of the test marine clay can be estimated. The PI of the marine clay is 35, and its degradation curve is shown in Figure 10. Compared to the uncemented marine clay, the E/E_0 values of the cemented specimens are generally higher. However, the difference between cemented and uncemented specimens reduces with increasing strain. The primary reason is that cement hydration products bond soil particles together, significantly enhancing soil stiffness (Clough et al. 1981). At smaller strains (strain < 0.01%), the specimen retains considerable cementation strength. For example, at a strain of 0.01%, the reduction in modulus is less than 10%, indicating a relatively lower rate of modulus degradation compared to uncemented clay. However, as the strain increases, the generation of plastic volumetric and deviatoric strain (Suebsuk et al. 2010; Jiao and Zhou 2024) leads to the deterioration of the cemented structure. Consequently, with increasing strain, the rate of modulus degradation progressively rises, eventually reaching a level comparable to that of clay."

Mechanisms for the influence of curing temperature

Figure 11 shows an in-depth investigation of the mechanism of curing temperature, in which TG and differential thermogravimetry (DTG) curves of the cemented marine clay at different curing temperatures are presented, with the mass loss of various components. Specifically, the mass losses correspond to calcium silicate hydrate (C-S-H) (40-600°C), ettringite (AFt) (80-180°C), Friedel's salt (F's salt) (200-300°C) (Shen et al., 2017; Sun et al., 2023), calcium hydroxide (CH) (400-500°C), and calcite (600-800°C). Part of the data from the TG test shown in Figure 11 are summarized in Table 5. Based on the weight loss data in Table 5, it is evident that specimens cured at higher temperatures exhibit greater total weight loss in the TG test. Specifically, the total weight loss is 12.4% for specimens cured at 20°C, while it is 14.5% for specimens cured at 30°C, suggesting that more hydration products are

generated at higher curing temperatures.

The amount of CH, which is an important parameter for analysing the cementation effects, can be calculated following the approach of Scrivener et al. (2018) and Sun et al. (2024a):

$$CH(\%) = \frac{74}{18}(Wl_{(400-500)} - 0.8 * Wl_{MD(400-500)}) \quad (1)$$

where $CH(\%)$ represents the content of CH, $Wl_{(400-500)}$ and $Wl_{MD(400-500)}$ represent the total mass loss percentage of the cemented specimens and pure marine clay between 400-500°C, respectively. According to this equation, the CH content can be estimated as the total weight loss of cemented specimenss between 400-500°C minus the weight loss of uncemented specimens in the same temperature range. The coefficient of 0.8 accounts for the mass percentage of marine clay in cemented specimens (Sun et al., 2023).

The CH content of specimens cured at two different temperatures, calculated using Equation (1), is nearly identical, with values of 2.97% at 20℃ and 2.96% at 30℃. However, the results in Figure 11 indicate that the weight loss in the TGA test resulting from cement hydration for specimens cured at 20℃ is 3.27% (12.38%-9.11%), while for those cured at 30℃, it is approximately 5.37% (14.48%-9.11%). This suggests a 60% increase in cement hydration products. Theoretically, as one of the hydration products, CH content should increase with the total hydration products, meaning the CH content at 30℃ should be 1.6 times that at 20℃. The discrepancy between the experimental results and theoretical expectations indicates that the additional CH produced at 30℃ is consumed by other reactions. Given that CH is only consumed in pozzolanic reactions (Zhang et al. 2014), increasing the curing temperature can promote pozzolanic reactions, thereby generating more strength-enhancing products. The elevated curing temperatures promote pozzolanic reactions may be attributed to two reasons: (1) with an increase in the curing temperature, the rate of hydration increases, producing more calcium hydroxide that raises the pH value of the environment; (2) at a higher

temperature, silicates and aluminates are easier to dissociate to participate in pozzolanic reactions (Maltais and Marchand 1997; Zhang et al. 2014).

It is acknowledged that some minerals in the marine clay may participate in the cement hydration reaction, resulting in an underestimation of the CH content. Given that clay contains minerals with distinct decomposition temperatures, the weight loss observed between 400-500°C in uncemented marine clay is primarily attributed to the dehydroxylation of kaolinite, which decomposes between 450-650°C, while illite decomposes between 500-800°C and montmorillonite between 500-700°C. Since kaolinite is an inert component in clay that contributes negligibly to the cement hydration reaction (Mehta and Monteiro 2006; Talabi et al. 2012; Nawaz et al. 2022), the error due to the cement hydration reaction can be considered negligible.

Figure 12 shows the MIP test result. The specimen cured at 20°C showed a bimodal distribution curve, defining two peaks at pore radius of 180 and 0.14 μm. When the curing temperature is 30 and 40°C, the pore size distribution changes from bimodal to unimodal. The transition from a bimodal PSD to an unimodal distribution is largely dependent on the curing temperature. This phenomenon can be attributed to two primary reasons. Firstly, an increase in curing temperature enhances the degree of cement hydration, resulting in a greater production of hydration products. Secondly, elevated curing temperatures promote the pozzolanic reaction, producing reticulated morphology compounds (calcium silicate and calcium aluminate) that can effectively improve the pore structure by covering and connecting the aggregates. As illustrated in the SEM image in Figure 7f, reticulated morphology compounds more effectively encapsulate the particle aggregates and fill the inter-aggregate pores.

The pore radius corresponding to the peak value of the density function decreases to 0.11 μm and 0.06 μm at 30 and 40°C, respectively. Generally, the density function for a pore

diameter smaller than 0.1 μm increases with higher curing temperatures, while the density function for a pore diameter larger than 0.1 μm decreases, indicating the growth of cementitious products fills the larger pores, consistent with the conclusions of (Horpibulsuk et al. 2009). The higher the curing temperature, the smaller the total infiltration volume. The experimental results show that the void ratio of cemented marine clay only decreases by 2% when the curing temperature increases from 20 to 40℃.

Influence of curing stress on the mechanical behaviour of cemented marine clay

Figure 13 illustrates the variation of UCS and E_{50} with curing stress. Both UCS and E_{50} show a significant increase with the rise in curing stress. As the curing stress increases from 0 to 300 kPa, the UCS nearly doubles, and the E_{50} increases by approximately 50%. The increase in UCS and E_{50} is attributed to the reduction in void ratio and the enhanced cementation bonds during curing, which have the most significant influence on the stability of the soil skeleton (Fernandez and Santamarina 2001), as demonstrated by the TG analysis and MIP test results detailed later. Moreover, the data indicates that with a curing temperature of 30°C, as the curing stress increases from 0 to 150 and 300 kPa, the UCS increases by 29% and 92%, respectively. With a curing temperature of 40°C, the UCS increases are 70% and 115% for the same increments in curing stress. These comparisons suggest that an increase in curing temperature magnifies the effects of curing stress. The higher the curing temperature, the more hydration products are produced, contributing to the effective bonding between soil particles. This, in turn, amplifies the effect of curing stress on the cementation bonds.

Figure 14 illustrates the stiffness degradation curves of specimens subjected to different curing stresses. As the strain increases, the Young's modulus of the specimens rapidly decreases, reaching approximately 25% of its maximum value when the strain reaches 1%. Specimens subjected to higher curing stresses consistently exhibit higher modulus. For example, the elastic Young’s modulus of specimens cured at 300 kPa is 1.7 times that of

specimens cured at 0 kPa.

Figure 15 presents the normalized Young's modulus decay curve, demonstrating that as the curing stress increases, the elastic threshold strain decreases and the rate of stiffness degradation increases. The difference is minor for specimens cured at 150 and 300 kPa. Compared to pure clay, the stiffness of cemented marine clay exhibits a slower degradation rate within a smaller strain range. At 1% strain, the normalized modulus degradation curve of the cemented marine clay converges with that of pure marine clay. This trend is consistent with the results of Subramaniam and Banerjee (2020) for specimens under low confining pressure. The results suggest that the bonding between soil particles influences the nonlinearity of stiffness. The elastic threshold strain decreases with increasing curing stress because the higher curing stress leads to a refined pore structure of the specimens, as confirmed by the subsequent MIP test results. For the specimens with a refined pore structure, the cementation structure is more susceptible to damage as the strain increases. It may be because stiffness degradation is affected by both the destruction of the cementation structure and the rearrangement of soil particles. At relatively small strains, the destruction of the cementation structure is the major reason for stiffness degradation. When the strain is relatively large, the rearrangement of soil particles becomes the major reason for the stiffness degradation. As explained before, the stiffness degradation induced by particle rearrangement is comparable, so the normalized stiffness degradation rate with large E_0 decreases gradually.

Mechanisms for the influence of curing stress

TG analysis was conducted on the specimens under different curing stresses. In each test condition, this study conducted two TG analysis experiments, as shown in Figure 16. The TG curves for the first and second tests exhibit consistent trends, and the difference in the total weight loss is relatively small, with a maximum error of 2%. As shown in the figure, the TG test results of specimens cured with and without confinement are basically consistent. It

means there is no significant difference in the total amount and composition of the hydration product. The data shown in Table 5 indicates that the difference in the total amount of hydration products is less than 0.8% for specimens cured at stresses of 0 and 300 kPa, which suggests that curing stress has no obvious effects on the cement hydration reaction. Some studies (Cui and Fall 2016; Chen et al. 2021) pointed out that curing stress can facilitate cement hydration reactions. They explain that the increased curing stress squeezes out more free water in the specimen, which allows more contact between cement particles, thereby facilitating the cement hydration reaction. However, TG analysis results in Fig. 12 show that the curing stress effects on cement hydration differ from the findings of Cui and Fall (2016) and Chen et al. (2021). The reason for this difference may be due to different curing conditions. In the current study, the specimens were cured underwater, while Cui and Fall (2016) and Chen et al. (2021) cured specimens in the air. Compared to specimens cured in air, those cured underwater have sufficient free water to sustain the progress of the cement hydration reaction.

Figure 17 shows the MIP test results. As the curing stress increases, the pores are significantly compressed. The maximum pore diameter is less than 200 μm for the specimens curing with confinement, while the maximum pore diameter is greater than 200 μm for the specimens without confinement. The pore size density function exhibits an unimodal curve, and the pore size distribution is mainly concentrated in the range of 0.01 μm to 1 μm. When the curing stress increases from 0 to 300 kPa, the pore size density decreases with the increase of curing stress. The population pores diameters at 0, 150 and 300 kPa are 0.11 μm, 0.06 μm, and 0.05 μm, respectively, indicating that curing stress alters the pore structure inside the cemented marine clay. As shown in Figure 17, the pore size density corresponding to a pore diameter of 0.05-2 μm significantly decreases, while the density corresponding to a pore diameter of 0.005-0.05 μm slightly increases. According to the study of Sun et al.

(2024b), pores in the 5-50 nm range mainly represent inner-aggregate pores, while pores with diameters from 50 nm to 2 μm include inter-aggregate pores in kaolinite and C-S-H, as well as capillary pores (Zeng et al., 2012; Yu et al., 2016; Dewitte et al., 2022). Hence, the MIP results here suggest that increased curing stress compresses the aggregate pores, potentially contributing to the formation of a more stable cemented structure.

Calculation of the secant modulus of DCM materials

Different aspects of the small strain behaviour of cemented marine clay have been discussed in detail. The results can provide useful insights and data for theoretical modelling. From the perspective of engineering designs following current design methods, the stiffness of cemented soil is usually assumed to be constant with the use of E_{50} (Kitazume and Terashi 2013).

On the one hand, the test data shows that the corresponding strain for E_{50} typically falls in the strain range of 0.3% to 0.5%. When the strain increases to this range, the modulus decreases to about 30% of its initial value. This simplified approach of using E_{50} is not always appropriate. For example, E_{50} may be too conservative for DCM-supported embankment projects in which the encountered strains are mainly located within smaller strains (Phutthananon et al. 2023). In contrast, for deep excavation in DCM-treated ground (Meepon, et al. 2016), the strain could be much greater than 0.5%. The use of E_{50} could overestimate soil stiffness and underestimate the ground deformation. Therefore, the selection of modulus needs to be determined based on the expected strain values. If E_{50} is used, a correction factor should be applied.

On the other hand, it is crucial to estimate E_{50} accurately in the current engineering practices. Two approaches for determining the E_{50} value are described below. Approach 1 utilizes the empirical linear relationship between UCS and E_{50} from current design guidelines. For instance, both Bruce et al. (2013) and the SCDOT (2022) suggested that for the wet

mixing method, the E_{50} should be 300 times the UCS, whereas, for the dry mixing method, it should be 150 times the UCS. Based on these design guideline recommendations, Equation (2) was proposed:

$$E_{50} = kq_u \quad (2)$$

where k is the coefficient representing the linear relationship between E_{50} and the unconfined compressive strength (qu), which can be determined by curve fitting. To evaluate the performance of Equation (2), previously published data (Swasdi et al. 2007, Bushra and Robinson 2013, Mansour et al. 2015) were utilized, with a primary focus on studies of cemented clay.

Figures 18a and 18b compare the test results with the calculated results using Equation (2). The maximum discrepancy between the test data from this study and the calculated results from Equation (2) is around 40%. For data from the literature, the maximum error is approximately 100%. It is worth noting that in current engineering practice, the input parameters are mostly determined without considering the influence of curing temperature and stress (Bruce et al. 2013; SCDOT 2022). For cemented marine clay in the current study, the ratio of E_{50} to UCS is 280, which is close to the value recommended by guidelines (Bruce et al. 2013; SCDOT 2022) for the wet mix method. Therefore, Equation (2) could still be used as long as the increase in strength with curing temperature and stress is properly considered.

The above approach may be used in engineering practice to estimate E_{50}. However, the coefficient of determination R^2 between the calculated and measured results is low for some cemented soils. Hence, an alternative approach has been proposed in this study. The test results show that the stiffness of cemented soil is not only controlled by cementation but also affected by other factors, such as void ratio. So far, many formulas have been proposed to calculate the elastic shear modulus incorporating density, stress, and cementation effects. One

such equation was proposed by Jiao and Zhou (2024), as shown in equation (3):

$$G_0 = A(1+e)^{-1.3}\left(\left(\frac{p'+p_b}{p_r}\right)^{0.5} + n_c\left(\frac{p_b}{p_r}\right)^{0.5}\right) \quad (3)$$

where A and n_c are model parameters, e is the void ratio, p' *is* the effective mean stress, p_b is the bonding strength, and p_r is a reference pressure taken as 100 kPa here. Using a similar mathematic form and considering the mean effective stress corresponding to E_{50} is qu/6 in UC tests, the following equation is proposed for E_{50}:

$$E_{50} = A(1+e)^{-1.3}\left(\frac{q_u}{p_r}\right)^{0.5} \quad (4)$$

This alternative method can be used when accurate analysis is desired and more data is available. The comparison between the measured and predicted E_{50} using Equation (4) is shown in Figure 18. The parameters used are also included in the figures. Compared to Equation (2), Equation (4) provides better modulus prediction results. This significant improvement is due to the incorporation of the density effect and the use of a nonlinear equation for E_{50} calculation.

Summary and conclusions

As the curing temperature rises from 20 to 40°C, the UCS of cemented marine clay doubles. The strength increase is mainly attributed to the accelerated cement hydration and enhanced pozzolanic reactions resulting from the elevated curing temperature. In particular, the pozzolanic reaction produces more Calcium Silicate Hydrate gel, which significantly contributes to the strength gain. Furthermore, as the curing stress increases from 0 to 300 kPa, the UCS of cemented marine clay doubles. The increase in curing stress does not affect the cement hydration reaction. Instead, it primarily contributes to pore compression and the formation of more effective cementation structures.

E_0 increases by about 50% as the curing temperature rises from 20°C to 40°C and by 80% when the curing stress increases from 0 to 300 kPa. Accompanying the increase in curing temperature and stress is a decrease in the elastic threshold strain corresponding to the

modulus attenuation curve. The reduction of elastic threshodl strain is because the increase in curing temperature and stress leads to smaller pore sizes, as demonstrated by MIP test results. Specimens with smaller pores are more easily damaged with increasing deformation. With further strain increase, the modulus degradation curve of cemented clay initially maintains a high decay rate and then gradually slows down. When the strain reaches 1%, the stiffness converges to approximately 20% of the maximum value. This behaviour may be because, at larger strains, the cementation structure is significantly damaged, and particle rearrangement and pore compression may dominate the stiffness degradation.

As the curing temperature and stress increase, both E_{50} and UCS significantly rise, but their ratio remains relatively constant. For approximation, the linear equation recommended by design guidelines (i.e., E_{50} = 300UCS) can be used in engineering practice. Alternatively, the newly proposed nonlinear equation from this study can be used to predict E_{50} with a higher accuracy. This nonlinear equation incorporates the density effect and can improve prediction accuracy with a single parameter compared to the linear equation.

Although the effects of curing temperature and curing stress on the stress-strain and stiffness of cemented marine clay under unconfined compression have been well explored in this study, further studies are required to investigate the effects of curing stress and curing temperature on the behaviour of cemented soil under different stress paths, drainage conditions and different strain rates.

Data availability statement

All data, models, and code generated or used during the study appear in the submitted article.

Acknowledgements

The authors would like to thank the Research Grants Council (RGC) of the HKSAR for providing financial support through grant N_PolyU526/23. This work was also supported by

RISUD/PolyU under Grant 1-BBWS.

References

ASTM. 2013. *Standard practice for making and curing concrete test specimens in the laboratory*. ASTM C192. West Conshohoken, PA, USA.

ASTM. 2020. *Standard Practice for Classification of Soils for Engineering Purposes (Unified Soil Classification System)*. ASTM. D2487 West Conshohoken, PA, USA.

Bache, B. K. F., P. Wiersholm, P. Paniagua, and A. Emdal 2022. "Effect of Temperature on the Strength of Lime–Cement Stabilized Norwegian Clays." *J. Geotech. Geoenviron. Eng.* 148(3), 04021198.

Bergado, D., and G. Lorenzo. 2005. "Economical mixing method for cement deep mixing." *Innova. Grout. Soil Impro*. 1-10.

Bruce, M. E. C., R. R. Berg, G. M. Filz, M. Terashi, D. S. Yang, J. G. Collin, and S. Geotechnica. 2013. "Federal Highway Administration design manual: Deep mixing for embankment and foundation support." United States. Federal Highway Administation. Offices of Research & Development.

Bushra, I., and R. G. Robinson. 2013. "Effect of fly ash on cement admixture for a low plasticity marine soil." *Adv. Civ. Eng. Mater*. 2(1): 608-621.

Cardoso, R., D. Ribeiro, and R. Néri. 2017. "Bonding effect on the evolution with curing time of compressive and tensile strength of sand-cement mixtures." *Soils Found*. 57(4): 655-668.

Chen, S., A. Wu, Y. Wang, and W. Wang. 2021. "Coupled effects of curing stress and curing temperature on mechanical and physical properties of cemented paste backfill." *Constr. Build. Mater*. 273: 121746.

Cheung, H., C. Yan, C. Cheung, and A. Wong. 2022. "Deep Cement Mixing–The Experience in Tung Chung East Reclamation and Challenges Ahead." *AIJR Proceedings*, 348-360.

Clayton, C., and G. Heymann. 2001. "Stiffness of geomaterials at very small strains." *Géotechnique* 51(3): 245-255.

Clough, G. W., N. Sitar, R. C. Bachus, and N. S. Rad. 1981. "Cemented sands under static loading." *J. Geotech. Eng. Div*. 107(6): 799-817.

Consoli, N., G. Rotta, and P. Prietto. 2000. "Influence of curing under stress on the triaxial response of cemented soils." *Géotechnique* 50(1): 99-105.

Cui, L., and M. Fall. 2016. "Mechanical and thermal properties of cemented tailings materials at early ages: Influence of initial temperature, curing stress and drainage conditions."

554 *Constr*. *Build*. *Mater*. 125: 553-563.
555 Dewitte,C., A. Bertron, M. Neji, L. Lacarriere, and A. Dauzeres, 2022. “Chemical and
556 microstructural properties of designed cohesive M-S-H pastes.” *Materials* 15(2): 547.
557 El Kamash, W., J. Han, and F. Asce. 2014. "Displacements of column-supported
558 embankments over soft clay after widening considering soil consolidation and column
559 layout: Numerical analysis." *Soils Found*. 54(6): 1054-1069.
560 Fernandez, A., and J. Santamarina. 2001. "Effect of cementation on the small-strain
561 parameters of sands." *Can*. *Geotech*. *J*. 38(1): 191-199.
562 GEO (2023). Test Method for Unconfined Compressive Strength of Cement Stabilised Soil
563 Cores (GEO Report No. 365). Geotechnical Engineering Office, Civil Engineering
564 Department, Government of the Hong Kong SAR.
565 GeoSpec 3. 2001. “Model specification for soil testing.” Geotechnical Engineering Office,
566 Civil Engineering Department, Government of the Hong Kong SAR.
567 Han, J., K. Wang, J. Shi, and Y. Wang. 2014. "Influence of sodium aluminate on cement
568 hydration and concrete properties." *Constr*. *Build*. *Mater*. 64: 342-349.
569 Horpibulsuk, S., R. Rachan, and Y. Raksachon. 2009. "Role of fly ash on strength and
570 microstructure development in blended cement stabilized silty clay." *Soils Found*. 49(1):
571 85-98.
572 Huang, P., M. Patel, and A. Bobet. 2008. *Classification of Organic Soils*. Technical Report
573 FHWA/IN/JTRP-2008/2.Purdue University.
574 Ismail, M. A., H. A. Joer, W. H. Sim, and M. F. Randolph. 2002. "Effect of cement type on
575 shear behavior of cemented calcareous soil." *J. Geotech. Geoenviron. Eng.* 128(6): 520-
576 529.
577 Jamsawang, P., N. Yoobanpot, N. Thanasisathit, P. Voottipruex, and P. Jongpradist. 2016.
578 "Three-dimensional numerical analysis of a DCM column-supported highway
579 embankment." *Comput. Geotech.* 72: 42-56.
580 Jiao, K. F., and C. Zhou. 2024. "A Bounding Surface Model for Cemented Soil at Small and
581 Large Strains." *J. Geotech. Geoenviron. Eng.* 150(2): 04023136.
582 Liu, S. Y., Y. J. Du, Y. L. Yi, and A. J. Puppala. 2012. "Field investigations on performance of
583 T-shaped deep mixed soil cement column–supported embankments over soft ground." *J.*
584 *Geotech. Geoenviron. Eng.* 138(6): 718-727.
585 Maltais, Y., and J. Marchand 1997. " Influence of curing temperature on cement hydration
586 and mechanical strength development of fly ash mortars." *Cement Concrete. Res.* 27(7):
587 1009-1020.

588 Mansour, M., A. Samieh, and H. Matter. 2015. “Engineering properties of cement/lime-
589 stabilized Egyptian soft clay.” *Proc. IOP Conference Series: Earth and Environmental*
590 *Science*, IOP Publishing, 012041.
591 Marques, S. F. V., L. Festugato, and N. C. Consoli. 2021. "Stiffness and strength of an
592 artificially cemented sand cured under stress." *Granular Matter.* 23: 1-16.
593 Meepon, I., P. Voottipruex, and P. Jamsawang. 2016. "Behaviors of soil cement columns and
594 stiffened soil cement column wall in shallow excavation." *Lowl Technol Int 18*(*3, Dec*):
595 197–208.
596 Mehta, P. K., and Monteiro, P. 2006. “Concrete: microstructure, properties, and materials.”
597 McGraw-Hill..
598 Melentijevic, S., J. Arcos, and C. Oteo. 2013. "Application of cement deep mixing method
599 for underpinning." *Proc., Proc. 18th Int. Conf. Soil Mech. Geotech. Eng.*, 2549-2552.
600 Nawaz, S., M. Ahmad, S. Asif, J. J. Klemeš, M. Mubashir, M. Munir, M. Zafar, A. Bokhari, A.
601 Mukhtar, and S. Saqib. 2022. "Phyllosilicate derived catalysts for efficient conversion of
602 lignocellulosic derived biomass to biodiesel: A review." *Bioresource Technol.* 343:
603 126068.
604 Ng, C. W. W., Zhou, C., & Ni, J. J. (2024). Advanced Unsaturated Soil Mechanics: Theory
605 and Applications. CRC Press.
606 Phutthananon, C., P. Jongpradist, A. Wonglert, K. Kandavorawong, S. Sanboonsiri, and P.
607 Jamsawang. 2023. "Field and 3D Numerical Investigations of the Performances of
608 Stiffened Deep Cement Mixing Column-Supported Embankments Built on Soft Soil."
609 *Arab. J. Sci. Eng.* 48(4): 5139-5169.
610 Pongsivasathit, S., W. Petchgate, S. Horpibulsuk, and S. Piyaphipat. 2021. "Composite
611 contiguous pile wall and deep mixing column wall as a dam–Design, construction and
612 performance." *Case Stud. Constr. Mater.* 15: e00771.
613 Ribeiro, D., R. Néri, and R. Cardoso. 2016. "Influence of water content in the UCS of soil-
614 cement mixtures for different cement dosages." *Procedia Eng.* 143: 59-66.
615 SCDOT 2022. "Geotechnical Design Manual." South Carolina Department of Transportation.
616 Scrivener, K., R. Snellings, and B. Lothenbach. 2018. A practical guide to microstructural
617 analysis of cementitious materials, Crc Press.
618 Shen, P., L. Lu, Y. He, F. Wang, and S. Hu. 2017. “Hydration of quaternary phase-gypsum
619 system.” *Constr. Build. Mater.* 152: 145-153.
620 Subramaniam, P., and S. Banerjee. 2020. "Dynamic properties of cement-treated marine
621 clay." *Int. J. Geomech.* 20(6): 04020065.

Subramanian, S., Q. Khan, and T. Ku. 2020. "Effect of sand on the stiffness characteristics of cement-stabilized clay." *Constr. Build Mater.* 264: 120192.

Suebsuk, J., S. Horpibulsuk, and M. D. Liu. 2010. "Modified Structured Cam Clay: A generalized critical state model for destructured, naturally structured and artificially structured clays." *Comput. Geotech.* 37(7-8): 956-968.

Sun, Z., W. B. Chen, R. D. Zhao, Y. F. Jin, and J. H. Yin. 2023. "Solidification/stabilization treatment of Hong Kong marine deposits slurry at high water content by ISSA and GGBS." *Constr. Build Mater.* 372: 130817.

Sun, Z., W. B. Chen, R. D. Zhao, N. Malik, J. H. Yin, and Y. Chen. 2024a. "Investigation on solidified/stabilized behavior of marine soil slurry by lime-activated incinerated sewage sludge ash-ground granulated blast furnace slag under multifactor conditions." *J. Rock Mech. Geotech. Eng*.

Sun, Z., W. B. Chen, R. D. Zhao, J. S. Li, Z. Y. Yin, J. H. Yin, and Y. G. Chen. 2024b. Physicochemical properties of clayey deposits slurry treated by lime-activated ISSA and GGBS considering seawater salinity effect. *Applied Clay Science, 248*, 107237.

Swasdi, S., S. Jaritngam, D. Tonnayopas, and P. Thongchim. 2007. "Soft Subgrade Stabilization with Cement in Satun Province, Thailand." *PSU-UNS International Conference on Engineering and Environment – ICEE. Phuket May.*

Talabi, A. O., O. L. Ademilua, and O. O. Akinola. 2012. "Compositional features and industrial application of Ikere kaolinite Southwestern Nigeria." *Research Journal in Engineering and Applied Sciences*, 1(5), 327-333.

Van Nguyen, S., L. S. Ho, and K. Nakarai. 2021. "Experimental Investigation of Cement Type Effect on Hydration and Strength Development of Cement-Treated Soils." *Proc., CIGOS, Emerging Technologies and Applications for Green Infrastructure: Proceedings of the 6th International Conference on Geotechnics, Civil Engineering and Structures*, Springer: 1045-1053.

Vardanega, P. J., and M. D. Bolton. 2013. "Stiffness of clays and silts: Normalizing shear modulus and shear strain." *J. Geotech. Geoenviron. Eng.* 139(9), 1575-1589.

Wang, Y., H. Dou, and G. X. Xie. (2019). "Stabilization of soft clay by deep cement mixing (DCM) method – A case study." *HKIE Transactions*.

Woo, S. 1971. "Cement and lime stabilization of selected lateritic soils." Thesis.

Yin, K., L. Zhang, H. Zou, H. Luo, and W. Lu. 2022. "Key factors for deep cement mixing construction for undredged offshore land reclamation." *J. Geotech. Geoenviron. Eng.* 148(8): 04022063.

Yin, K., T. Xiao, H. Luo, H. Zou, and L. Zhang. 2023. "Probabilistic modeling of offshore deep cement mixing improved ground." *Comput. Geotech.* 156: 105266.

Yu, C. Y., J. K. Chow, and Y. H. Wang. 2016. “Pore-size changes and responses of kaolinite with different structures subject to consolidation and shearing.” *Eng. Geol*. 202: 122-131.

Zeng, Q., K. F. Li, T. F. Chong, and P. Dangla. 2012. ”Pore structure characterization of cement pastes blended with high-volume fly-ash.” *Cem. Concr. Res.* 42: 194-204.

Zhang, R., Y. Lu, T. Tan, K. Phoon, and A. Santoso. 2014. "Long-term effect of curing temperature on the strength behavior of cement-stabilized clay." *J. Geotech. Geoenviron. Eng.* 140(8): 04014045.

Zhao, L., Y. Chen, W. Chen, J. Wang, and C. Ren. 2023. "The performance of T-shaped deep mixed soil cement column-supported embankments on soft ground." Constr. Build Mater. 369: 130578.

Click here to access/download;Table;Tables.docx

Table 1. Test program and main properties of each sample

Curing temperature, T_c (°C)	Curing stress, S_c (kPa)	Cement content, Cc (%)	Void ratio (after curing), e	q_u (MPa)	E_0 (MPa)	E_{50} (MPa)
20	0	15	1.68	1.16	816	478
		25	1.62	1.44	1080	675
		35	1.58	2.36	1292	770
30	0	15	1.67	1.60	1120	595
		25	1.60	2.28	1417	929
		35	1.56	2.78	1600	1037
	150	25	1.44	2.94	1890	1140
	300	25	1.27	4.38	2540	1310
40	0	15	1.65	2.32	1390	755
		25	1.54	2.84	1620	1020
		35	1.53	4.20	1780	1250
	150	25	1.42	4.88	2269	1455
	300	25	1.23	6.12	3081	1530

Table 2. Chemical compositions of the cement binder

Component	SiO_2	Fe_2O_3	Al_2O_3	CaO	MgO	SO_3
Percentage (%)	20.00	3.04	5.53	64.30	1.28	4.49

Table 3. Physical properties of the marine clay

Specific gravity	Liquid limit (%)	Plastic limit (%)	Plasticity index (%)	LOI (%)	Particle size distribution (%)		
					Sand content	Silt content	Clay content
2.62	63.9	28.2	35.7	4.31	16.7	61.0	22.3

Table 4. Tests to verify repeatability (with comparisons to those in Table 1)

Curing temperature, T_c (°C)	Curing stress, S_c (kPa)	Cement content, Cc (%)	Void ratio (after curing), e	q_u (MPa)	E_{50} (MPa)
20	0		1.68	1.01	439
	0		1.60	1.86	729
30	150		1.42	2.99	857
	300	25	1.30	4.00	1131
	0		1.53	2.72	911
40	150		1.45	4.64	1290
	300		1.28	6.19	1394

Table 5. Comparison of the weight loss for different specimens

Specimen	Curing temperature, T_c (°C)	Curing stress, S_c (kPa)	Weight loss (% of original)		CH content (%)
			400-500℃	0-1000℃	
Pure marine clay	/	/	1.62	9.11	/
Cemented marine clay	20℃	0 kPa	2.02	12.38	2.97
	30℃	0 kPa	2.01	14.48	2.96
	30℃	300 kPa	1.99	14.36	2.86

Click here to access/download;Figure;Figure 1.pdf

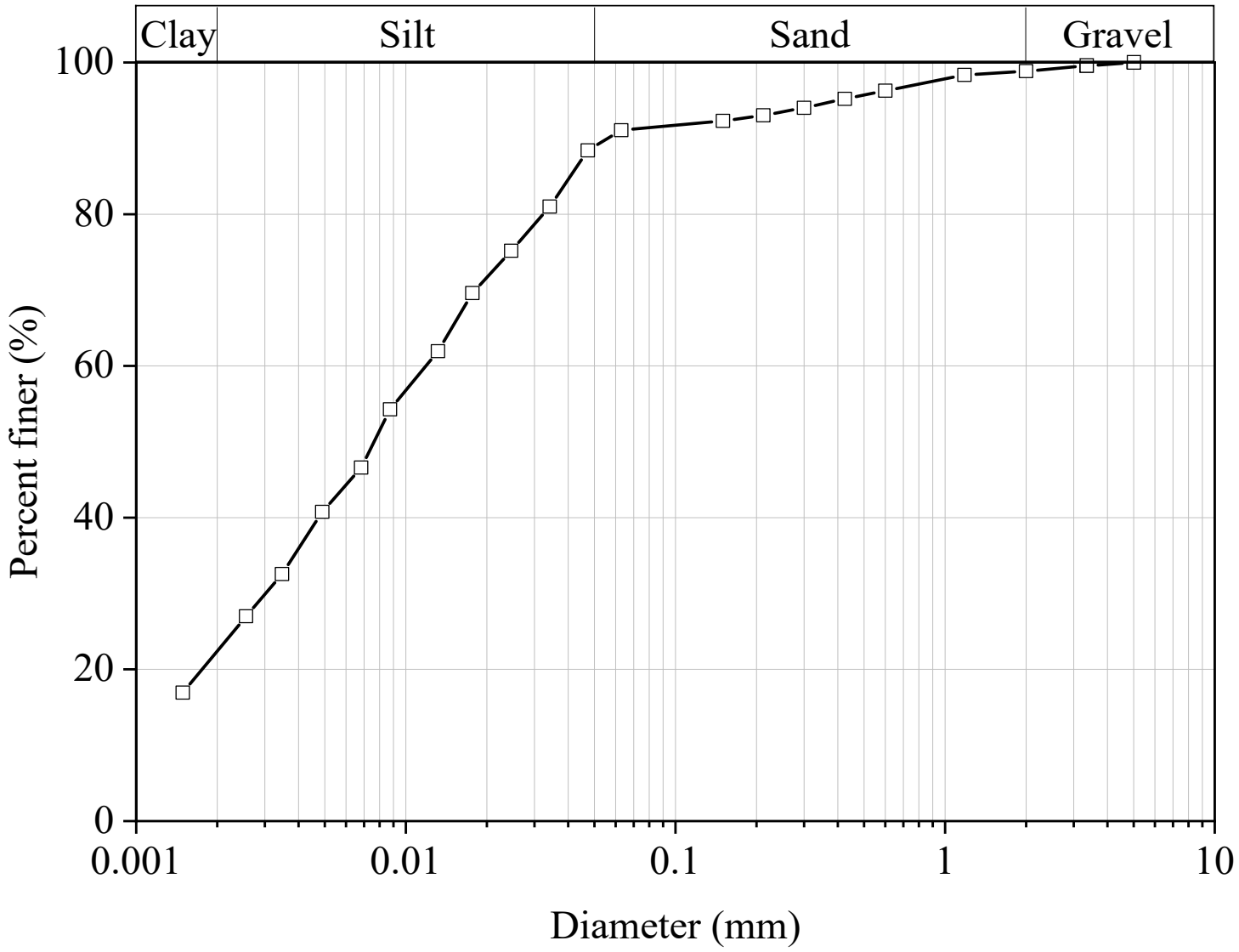

Click here to access/download;Figure;Figure 2a.pdf

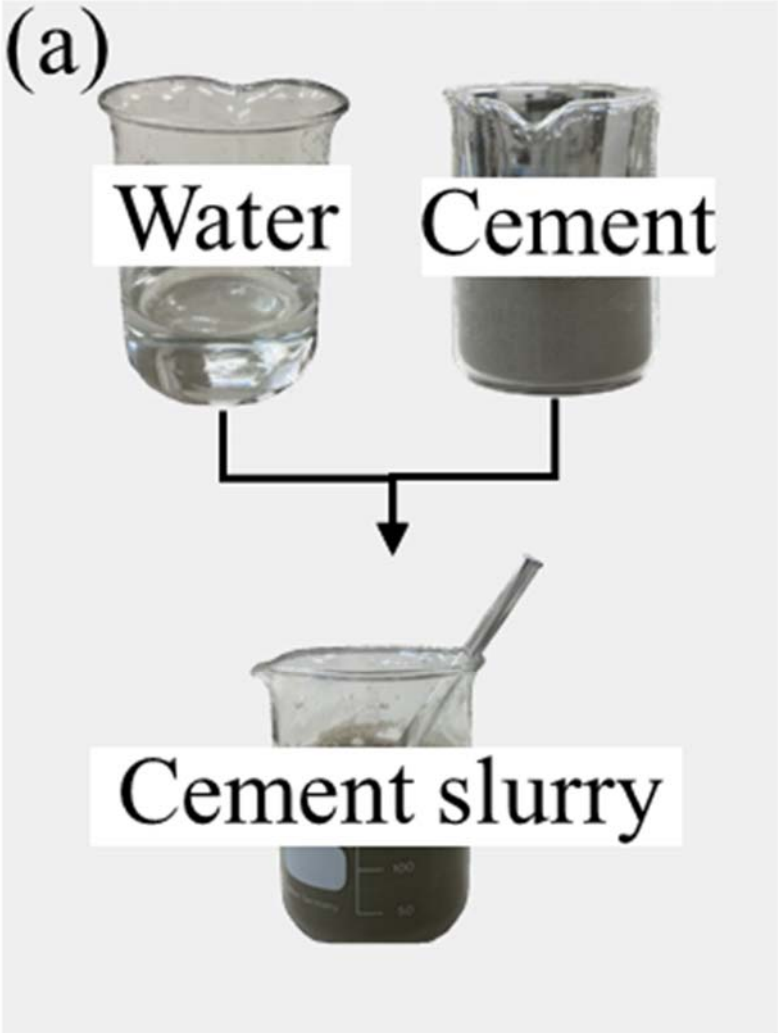

Click here to access/download;Figure;Figure 2b.pdf

Click here to access/download;Figure;Figure 2c.pdf

Click here to access/download;Figure;Figure 2d.pdf

(d)

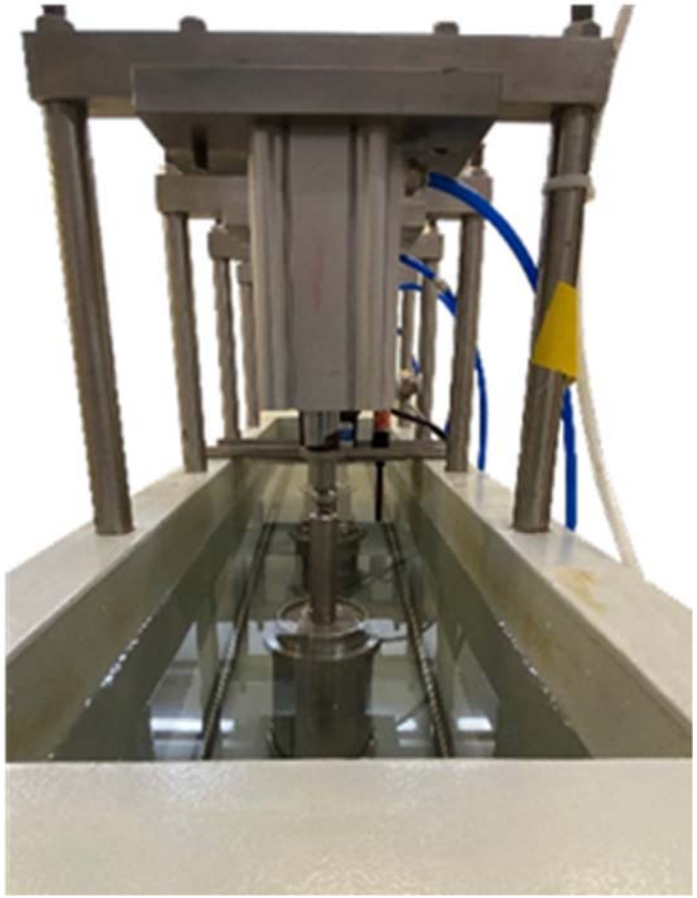

Click here to access/download;Figure;Figure 3a.pdf

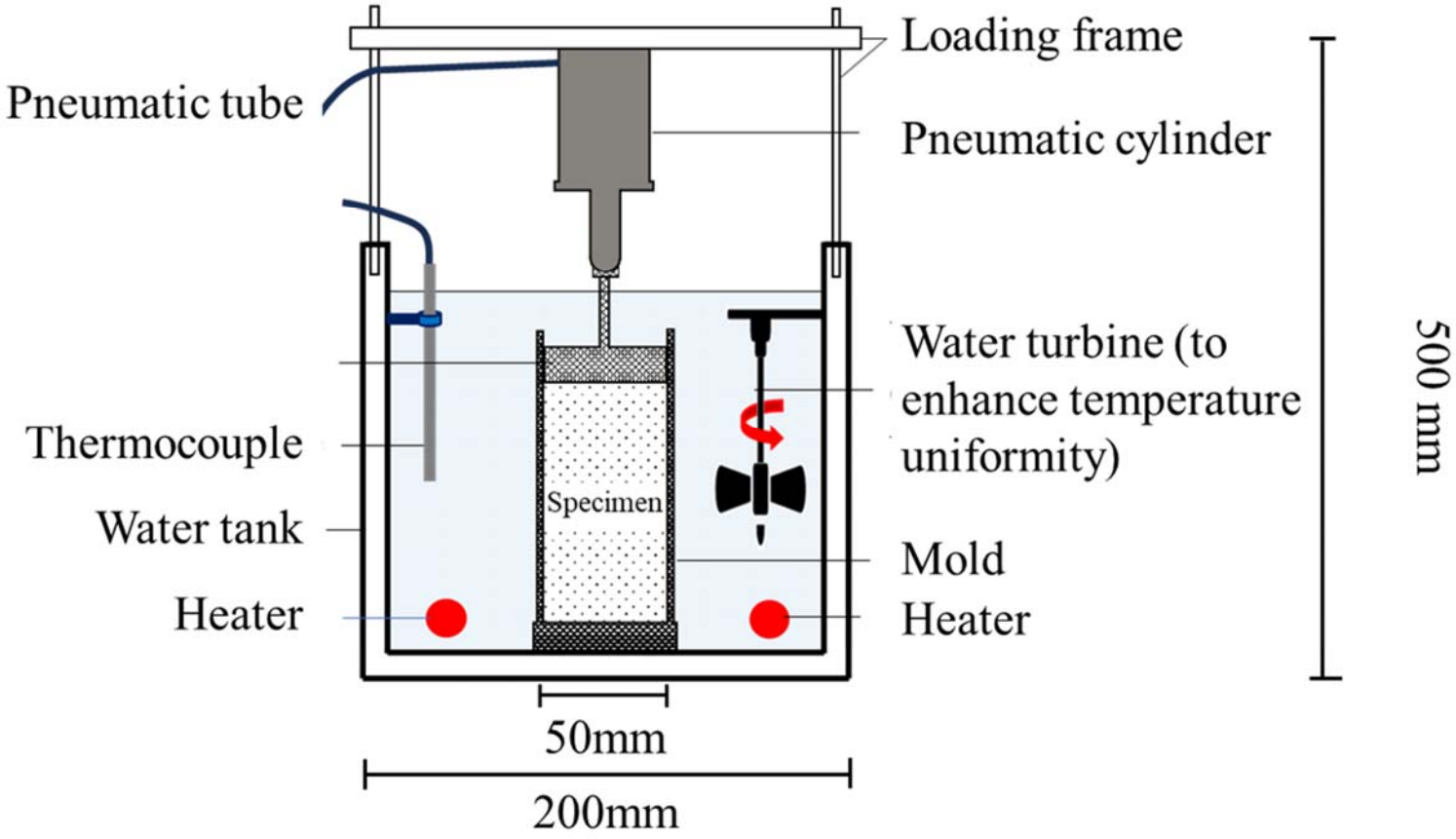

Click here to access/download;Figure;Figure 3b.pdf

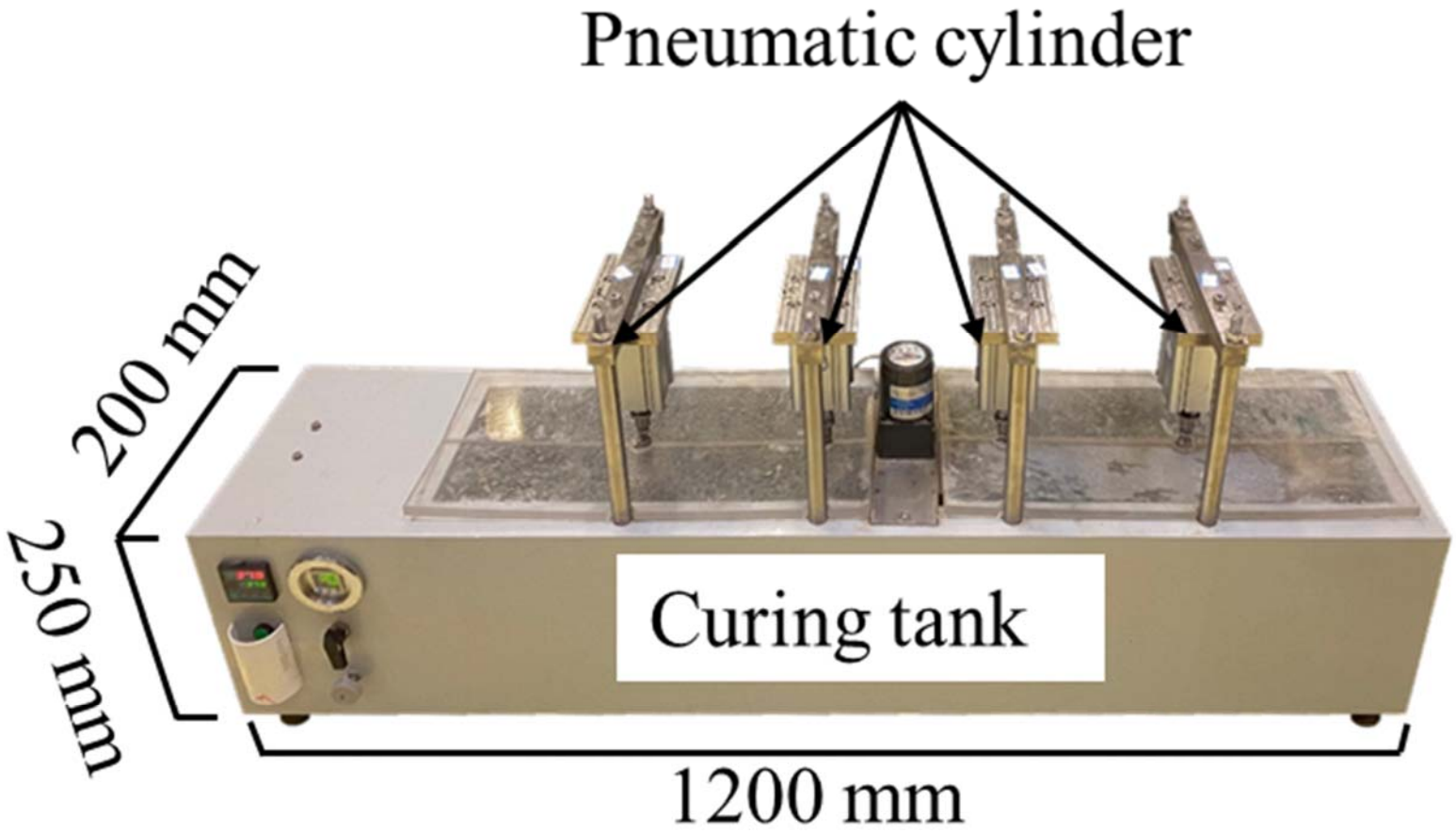

Click here to access/download;Figure;Figure 4.pdf

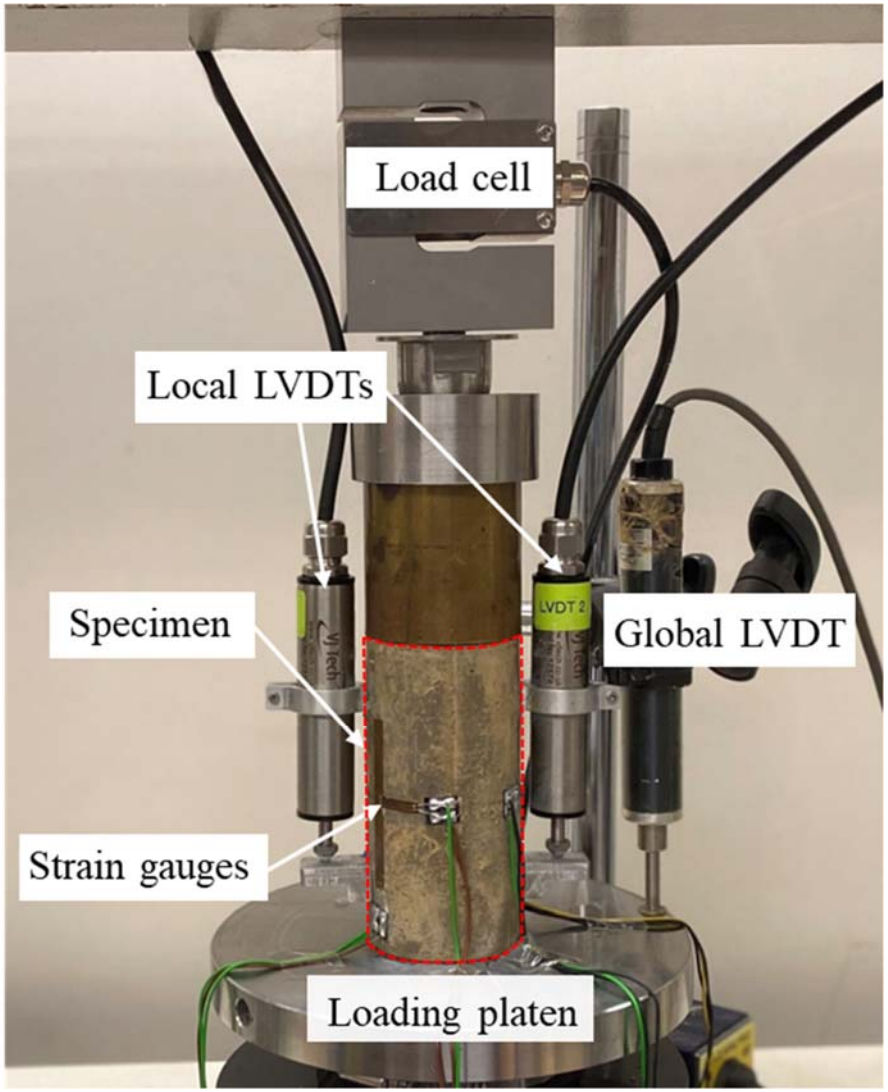

Click here to access/download;Figure;Figure 5.pdf

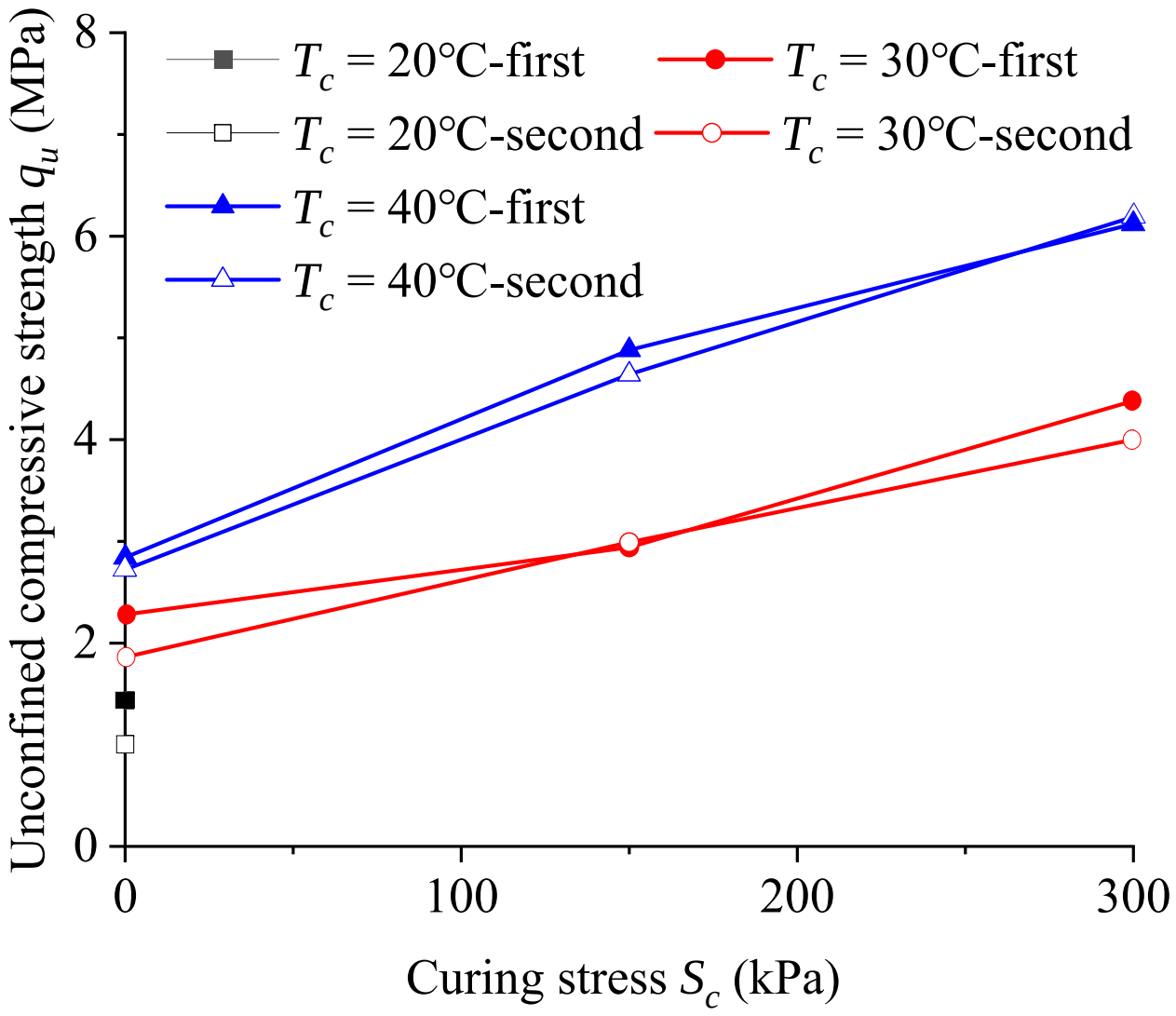

Click here to access/download;Figure;Figure 6a.pdf

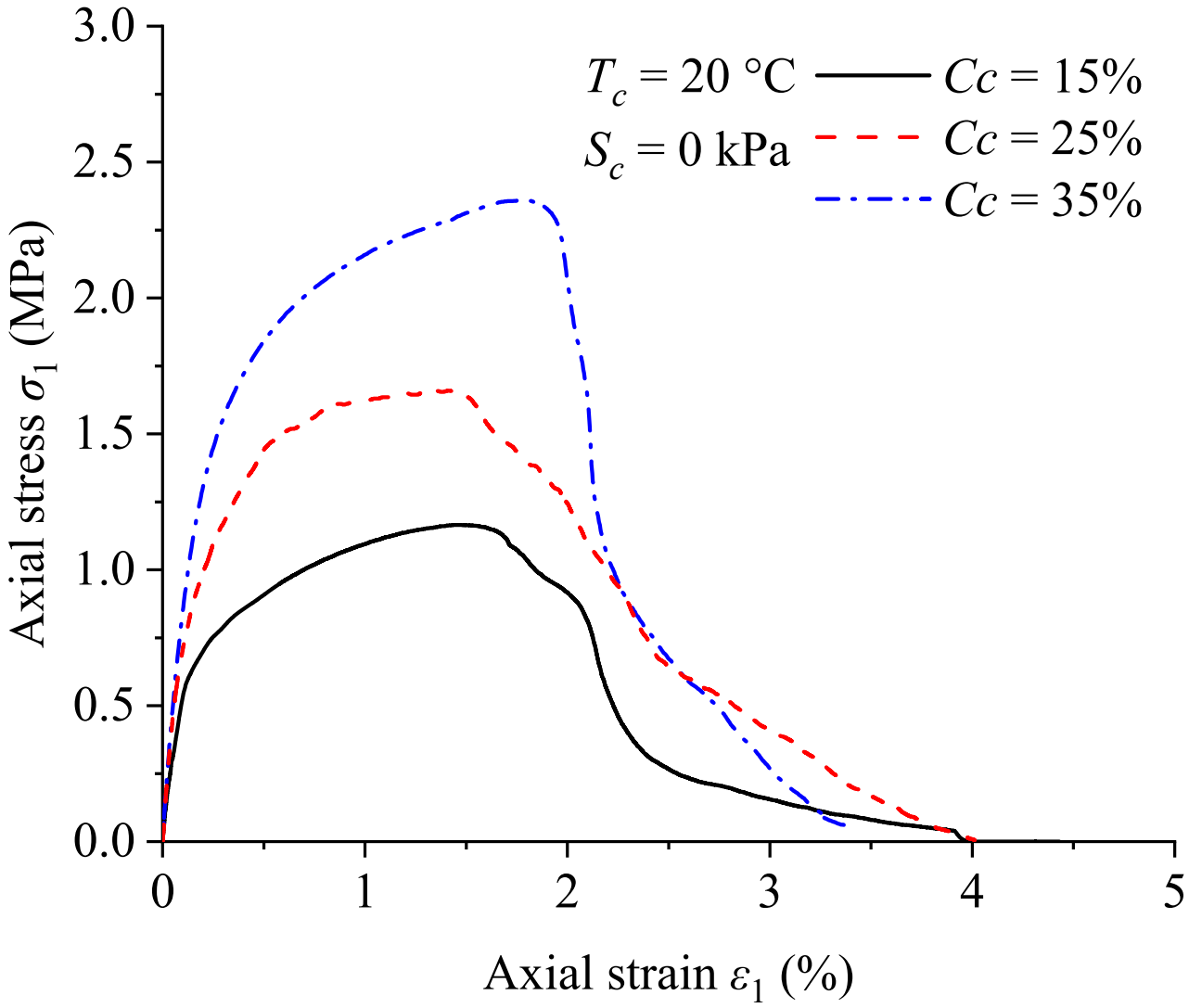

Click here to access/download;Figure;Figure 6b.pdf

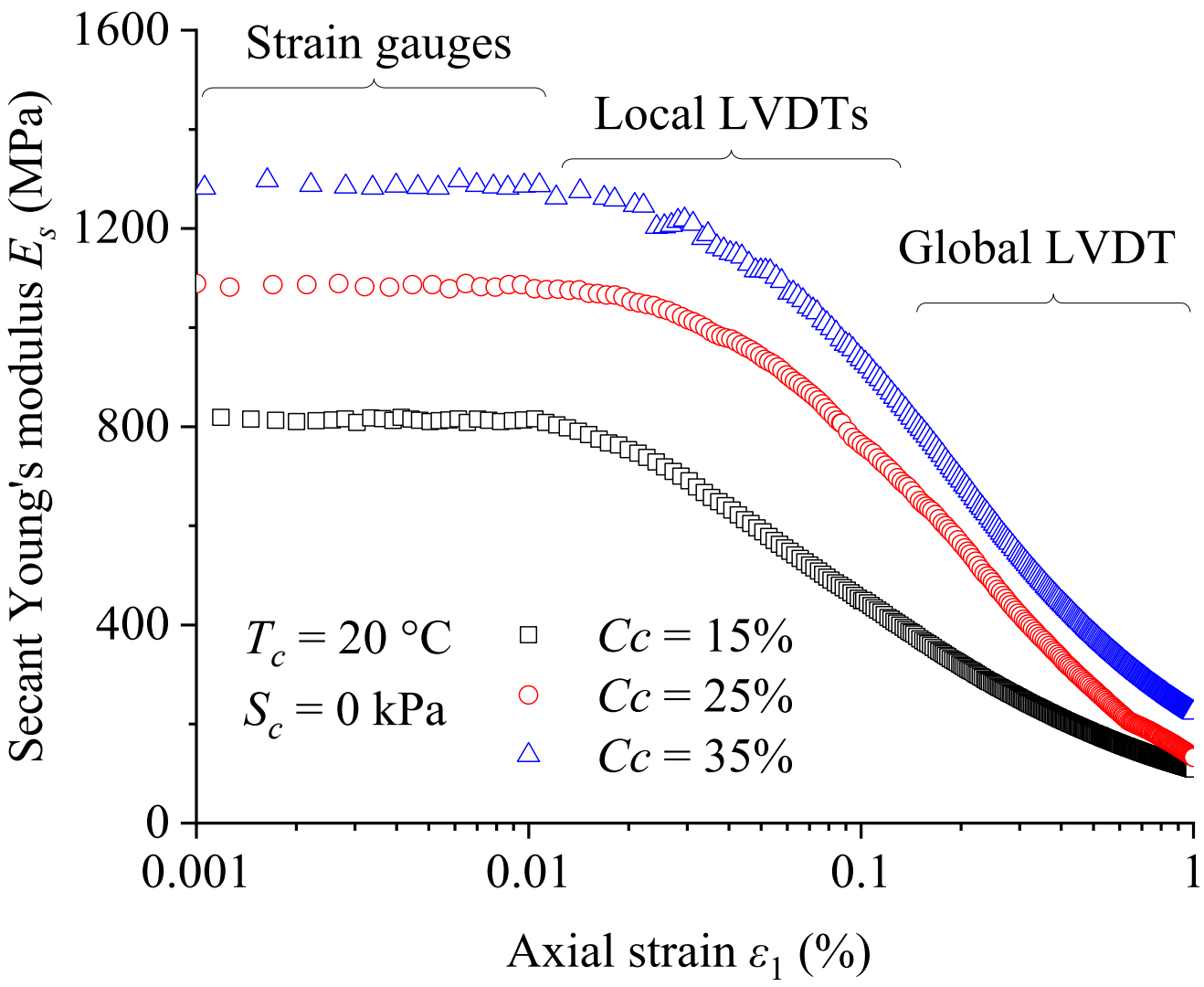

Click here to access/download;Figure;Figure 7a.pdf

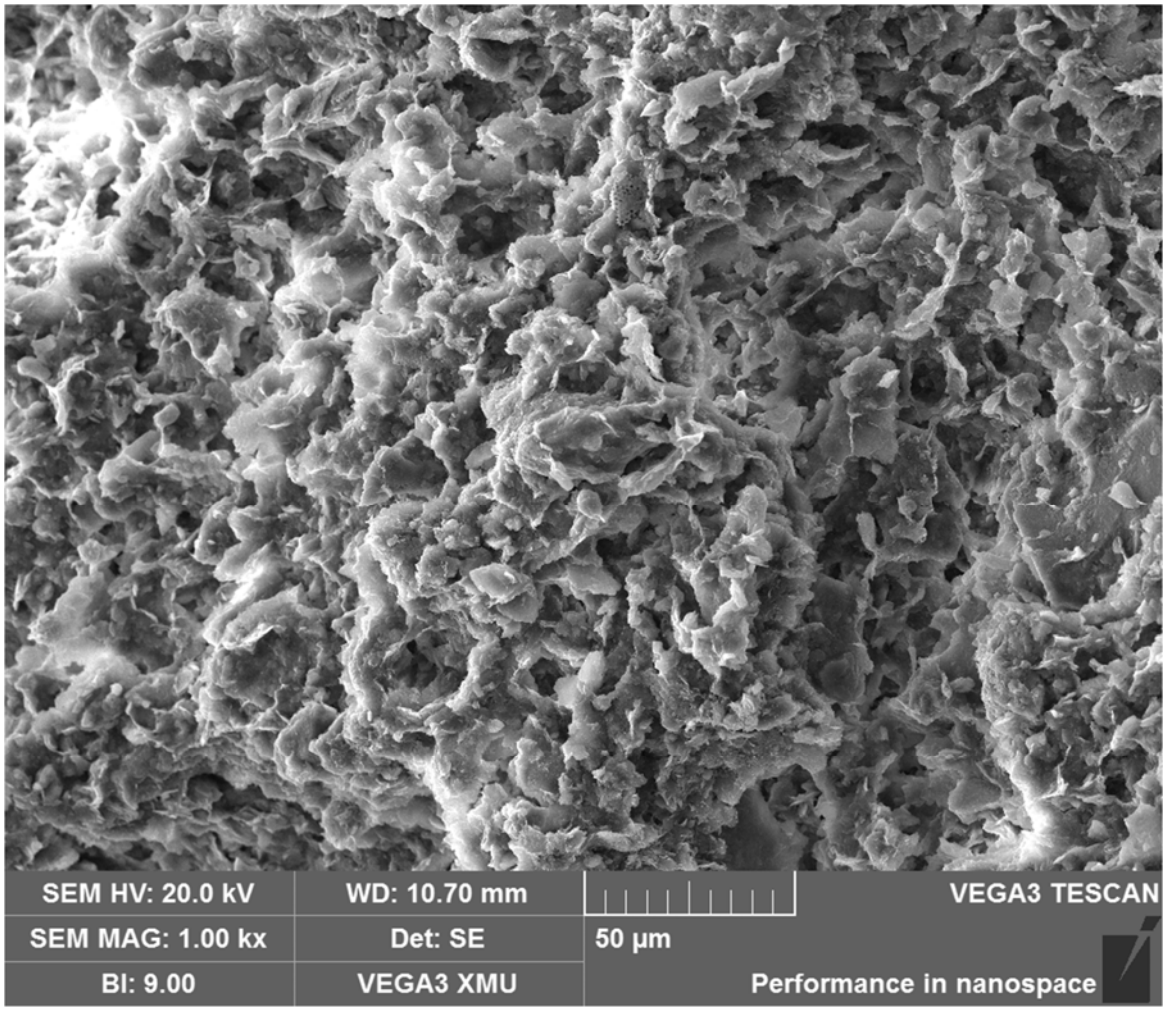

Click here to access/download;Figure;Figure 7b.pdf

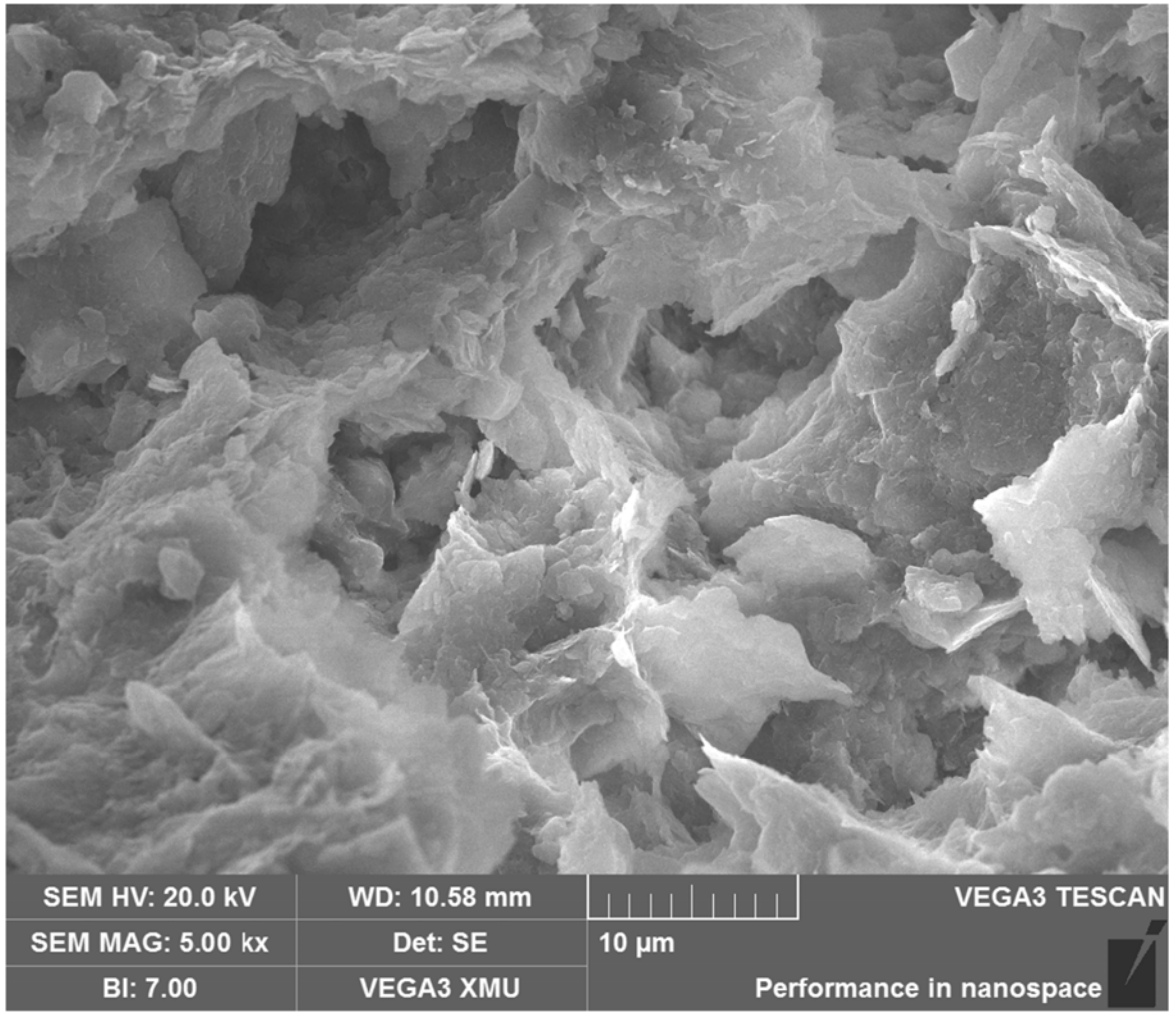

Click here to access/download;Figure;Figure 7c.pdf

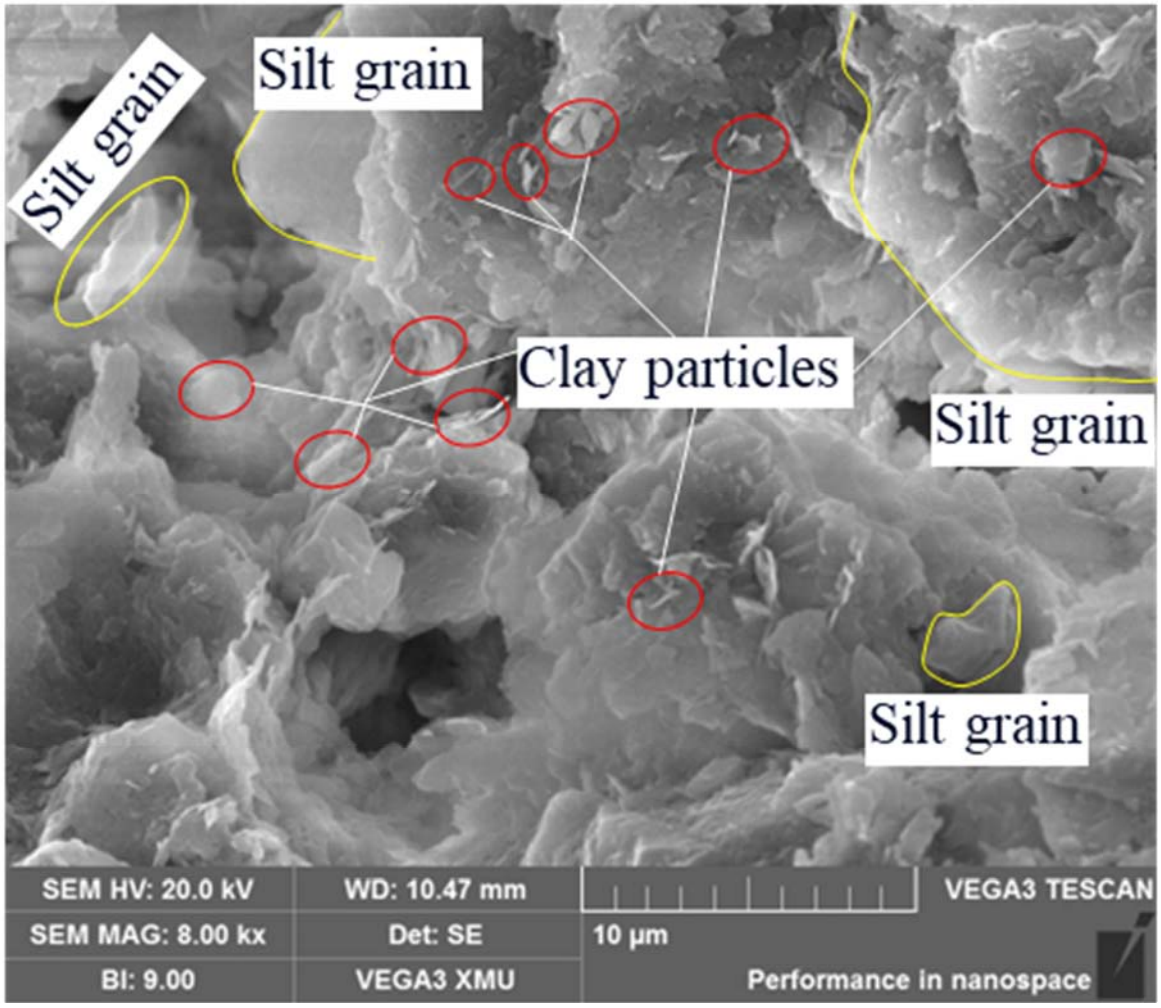

Click here to access/download;Figure;Figure 7d.pdf

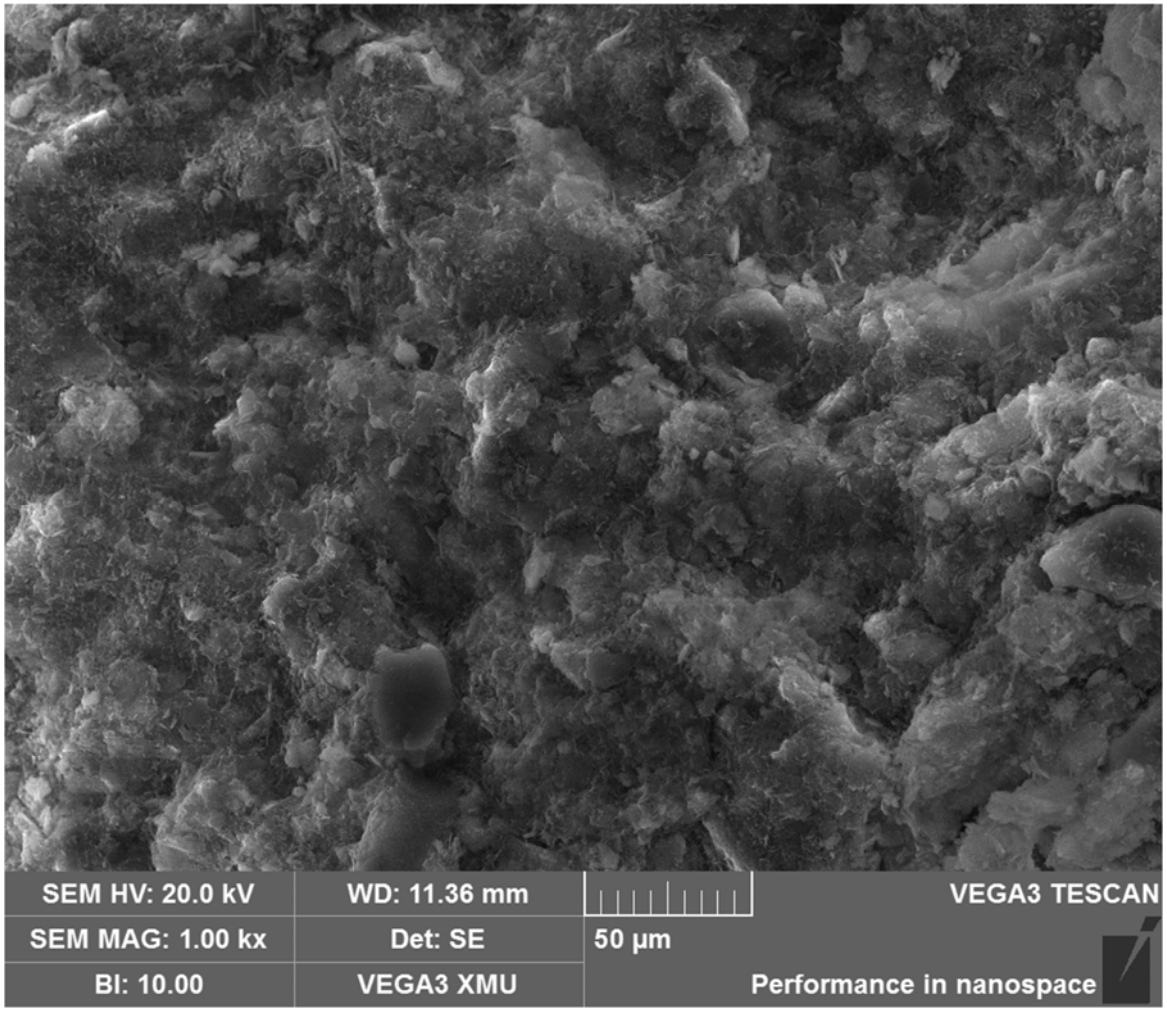

Click here to access/download;Figure;Figure 7e.pdf

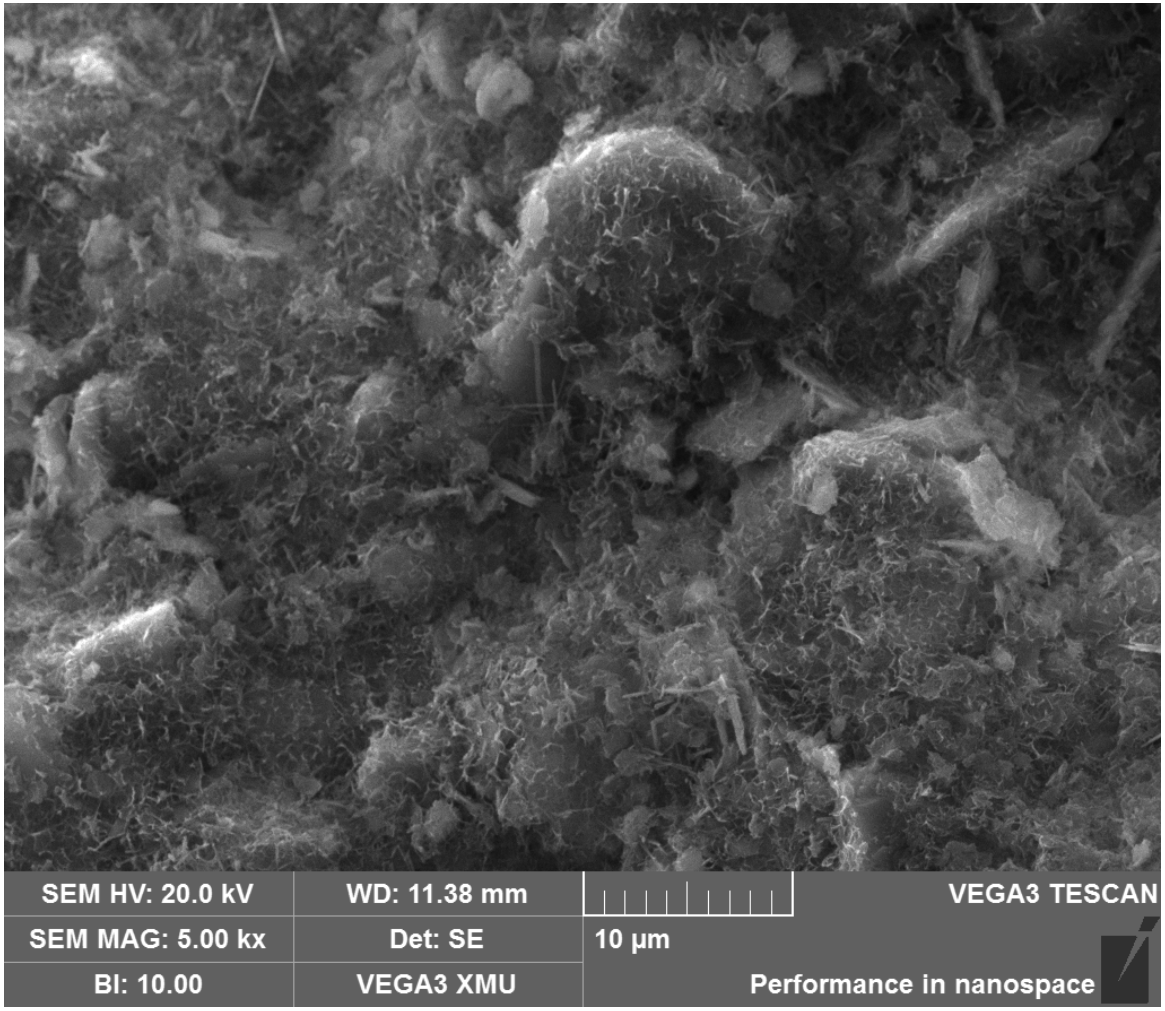

Click here to access/download;Figure;Figure 7f.pdf

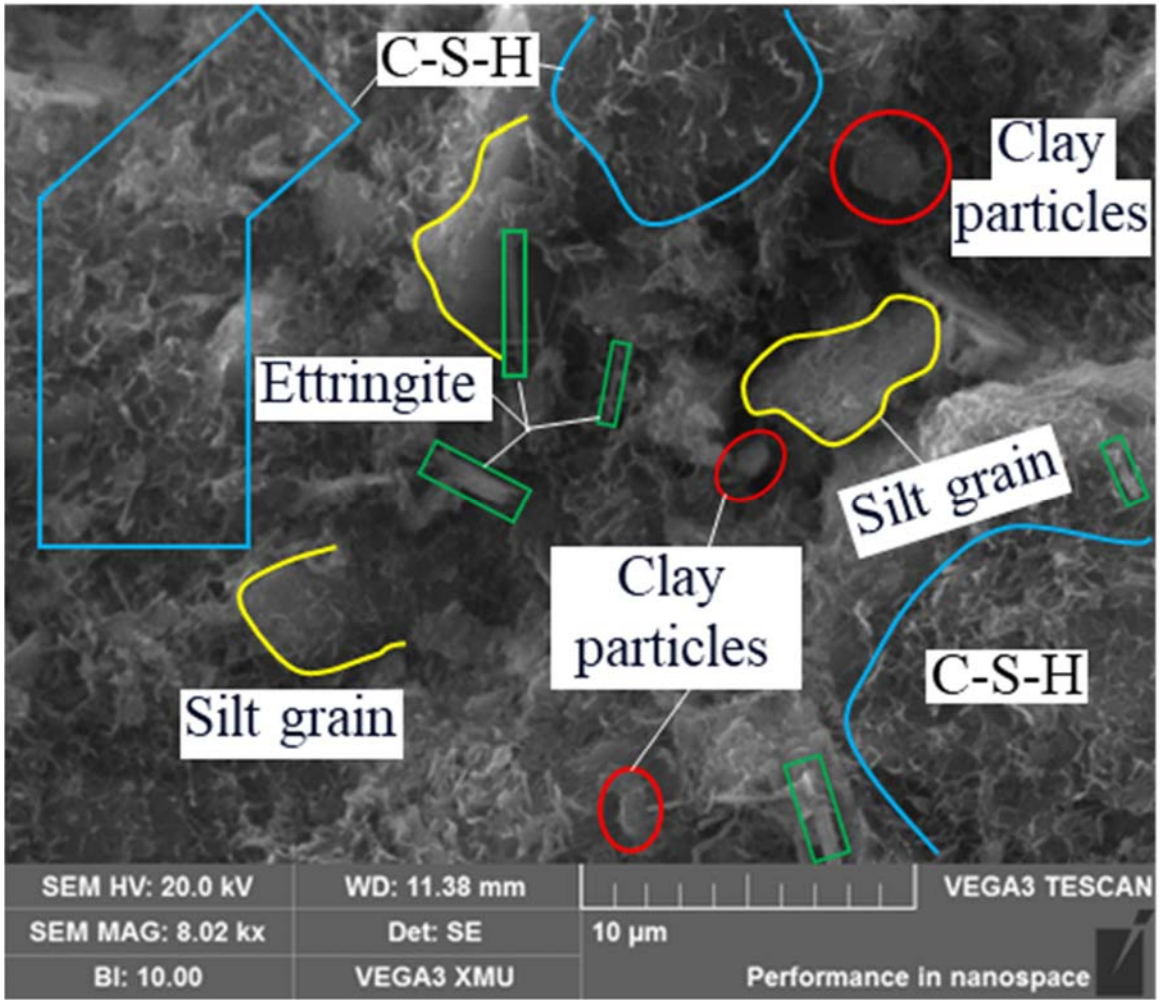

Click here to access/download;Figure;Figure 8a.pdf

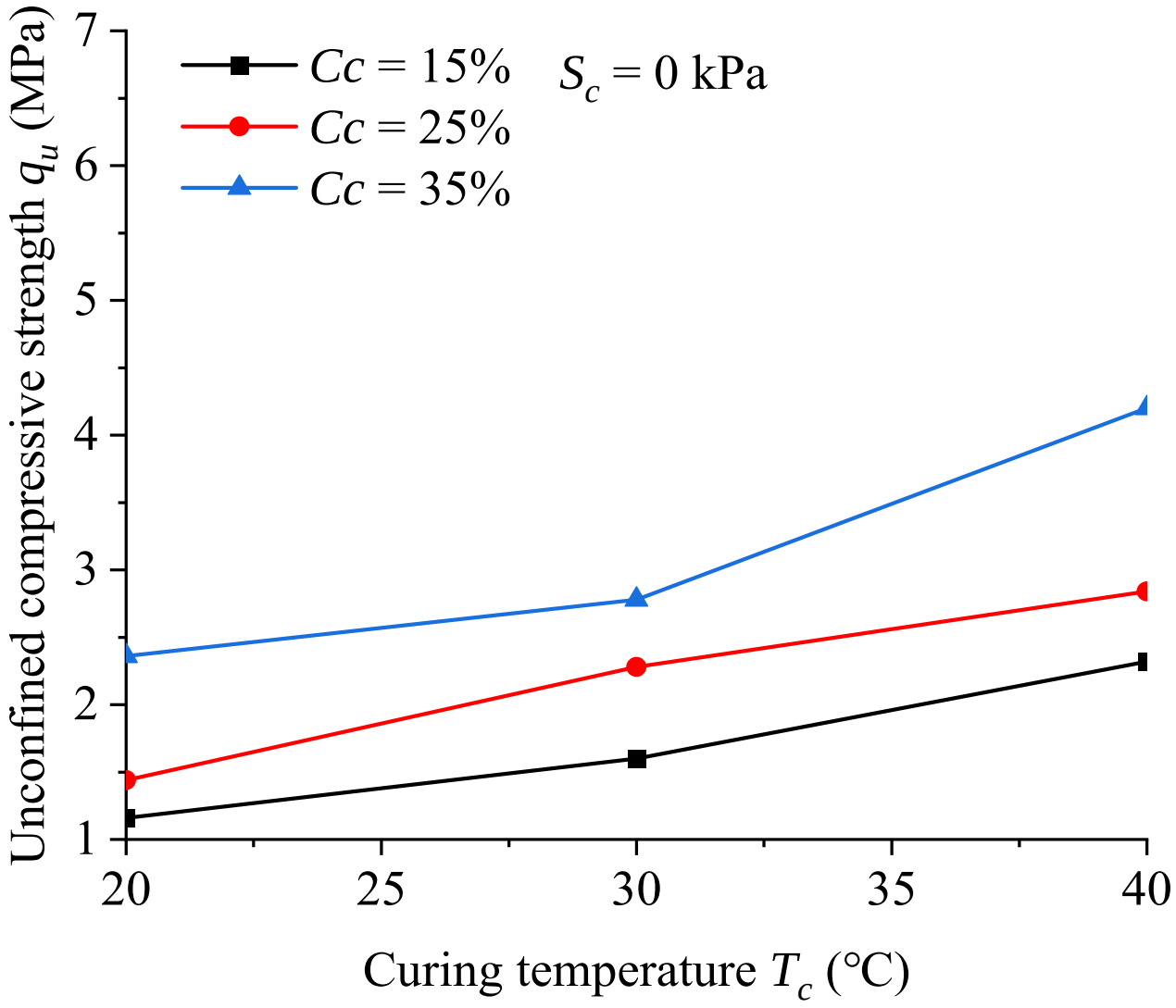

Click here to access/download;Figure;Figure 8b.pdf

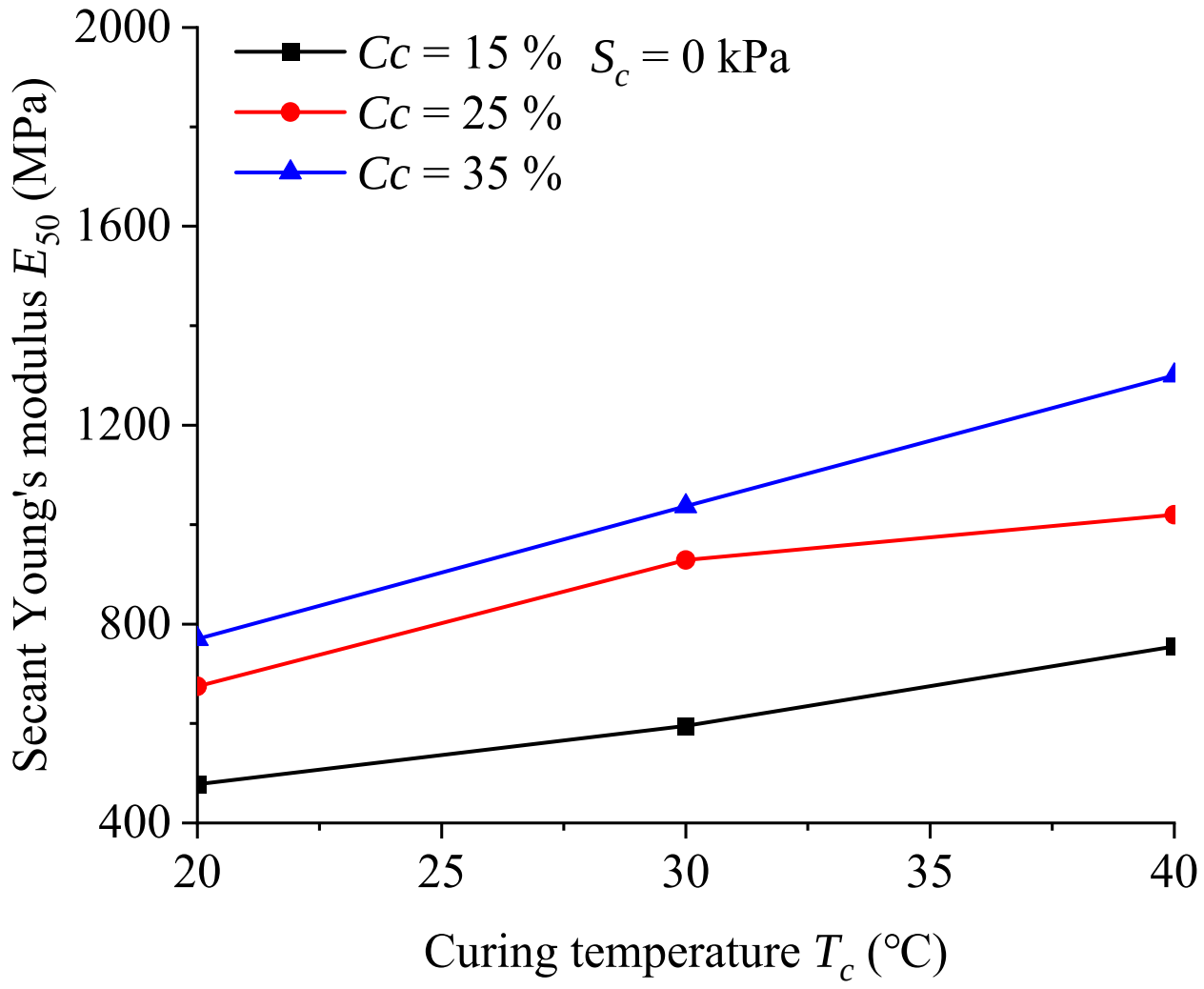

Click here to access/download;Figure;Figure 9a.pdf

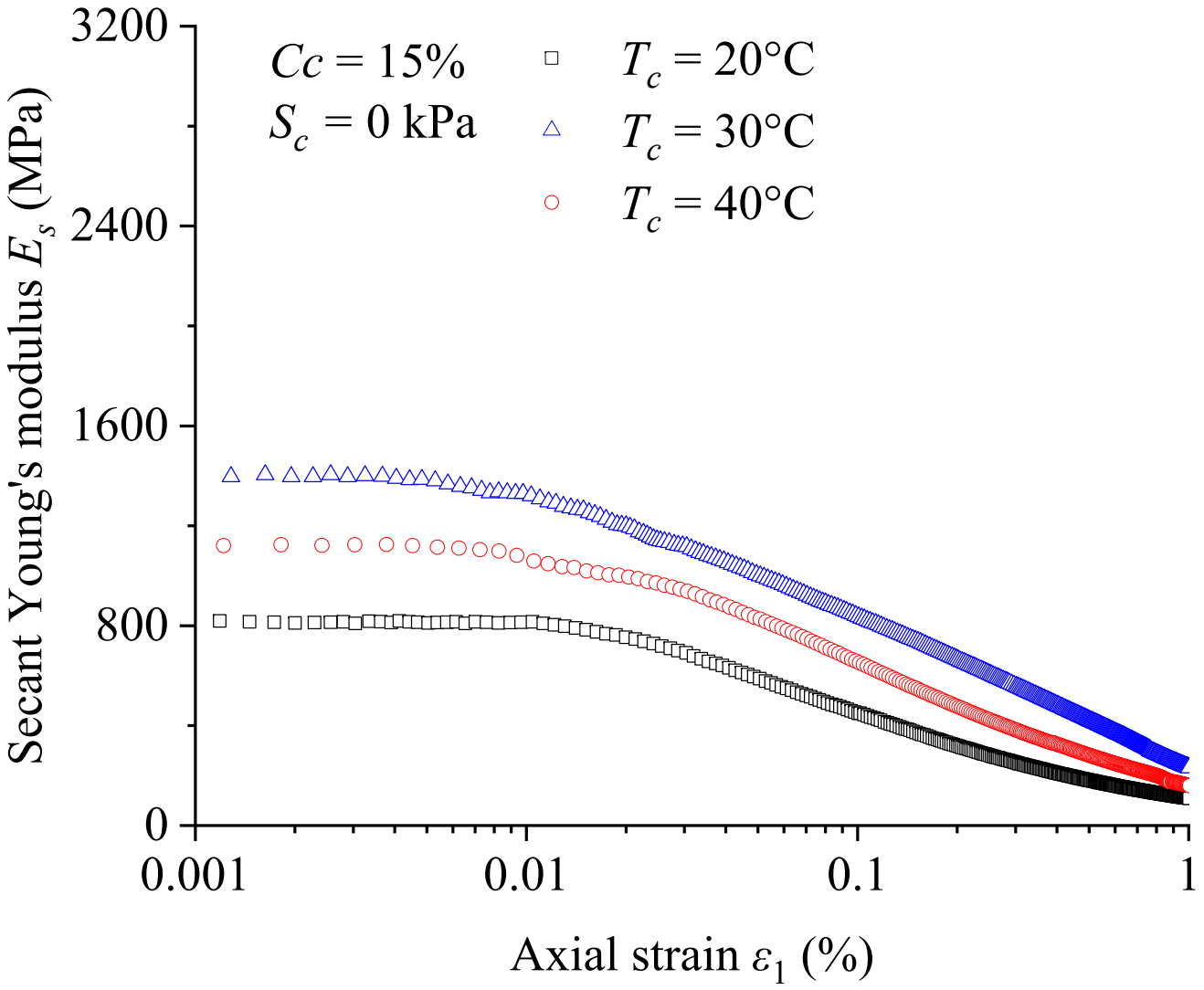

Click here to access/download;Figure;Figure 9b.pdf

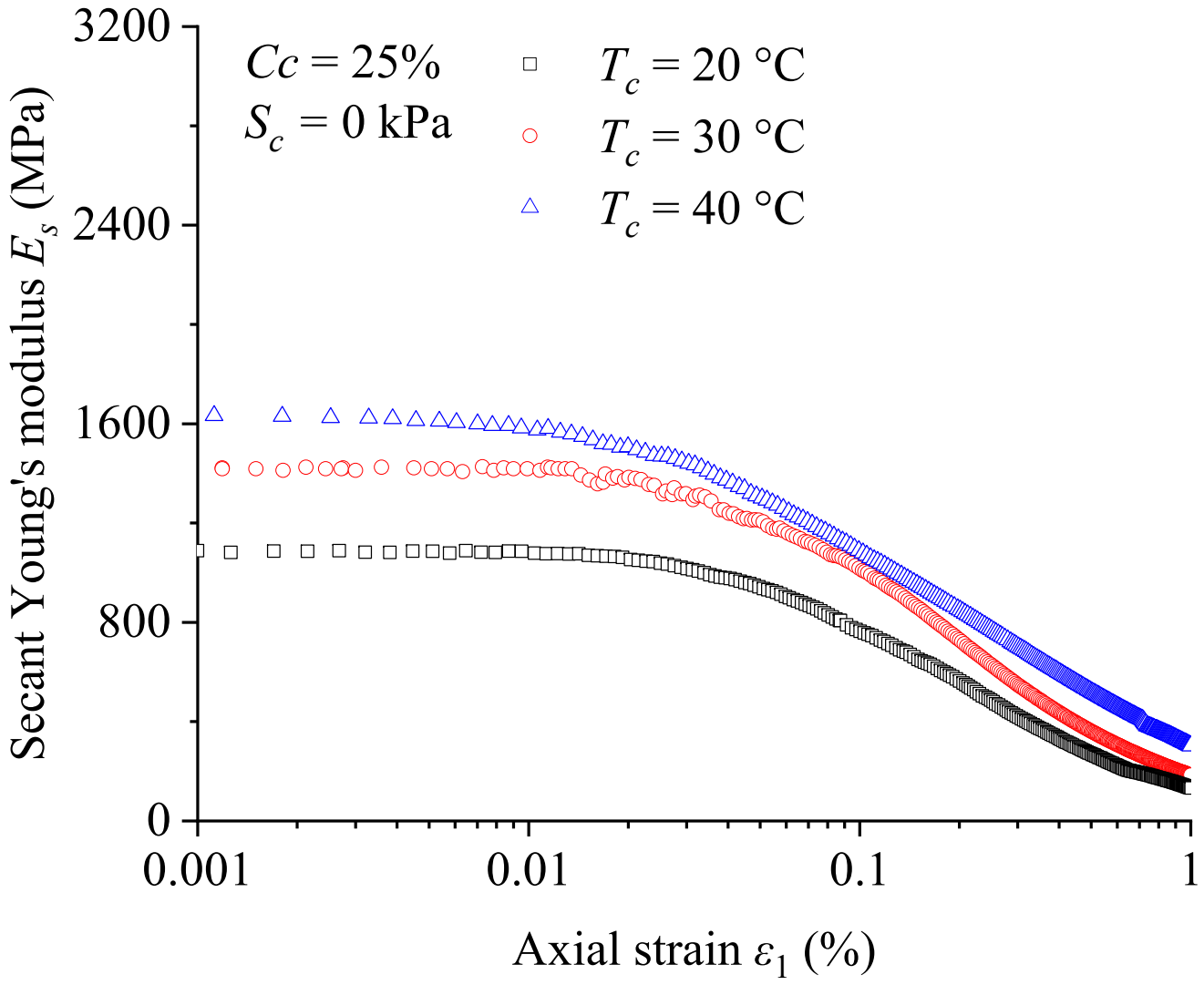

Click here to access/download;Figure;Figure 9c.pdf

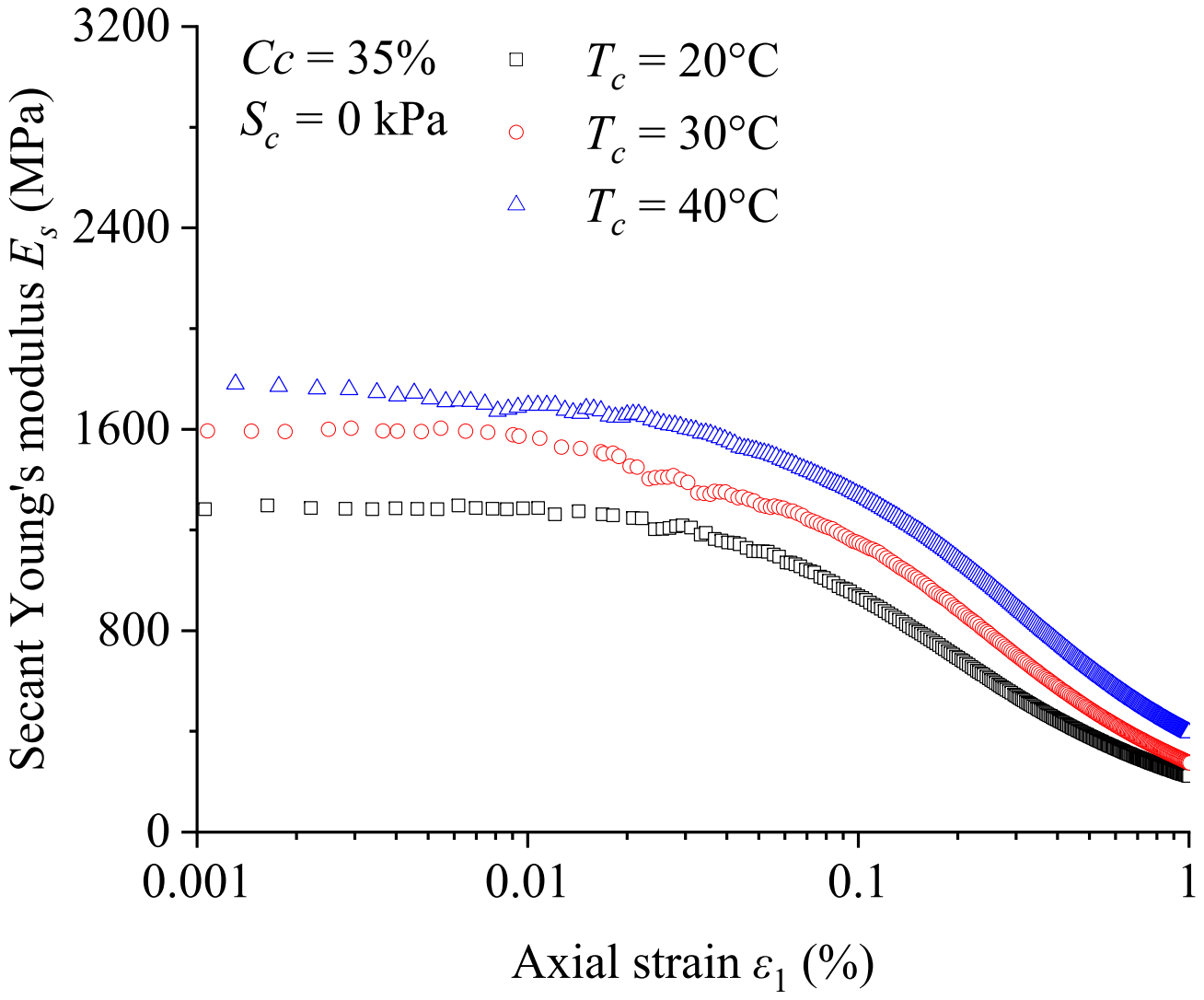

Click here to access/download;Figure;Figure 10.pdf

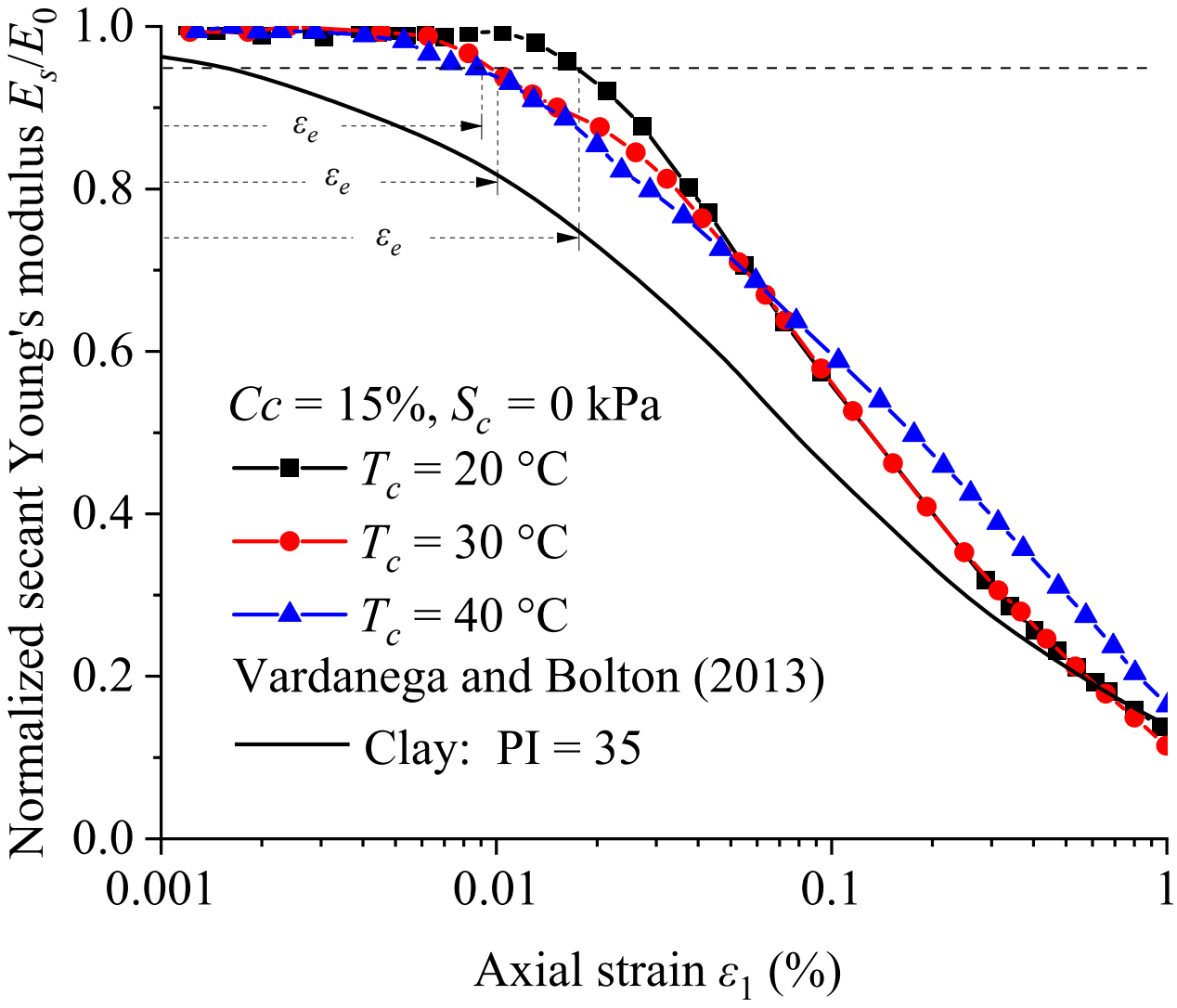

Click here to access/download;Figure;Figure 11a.pdf

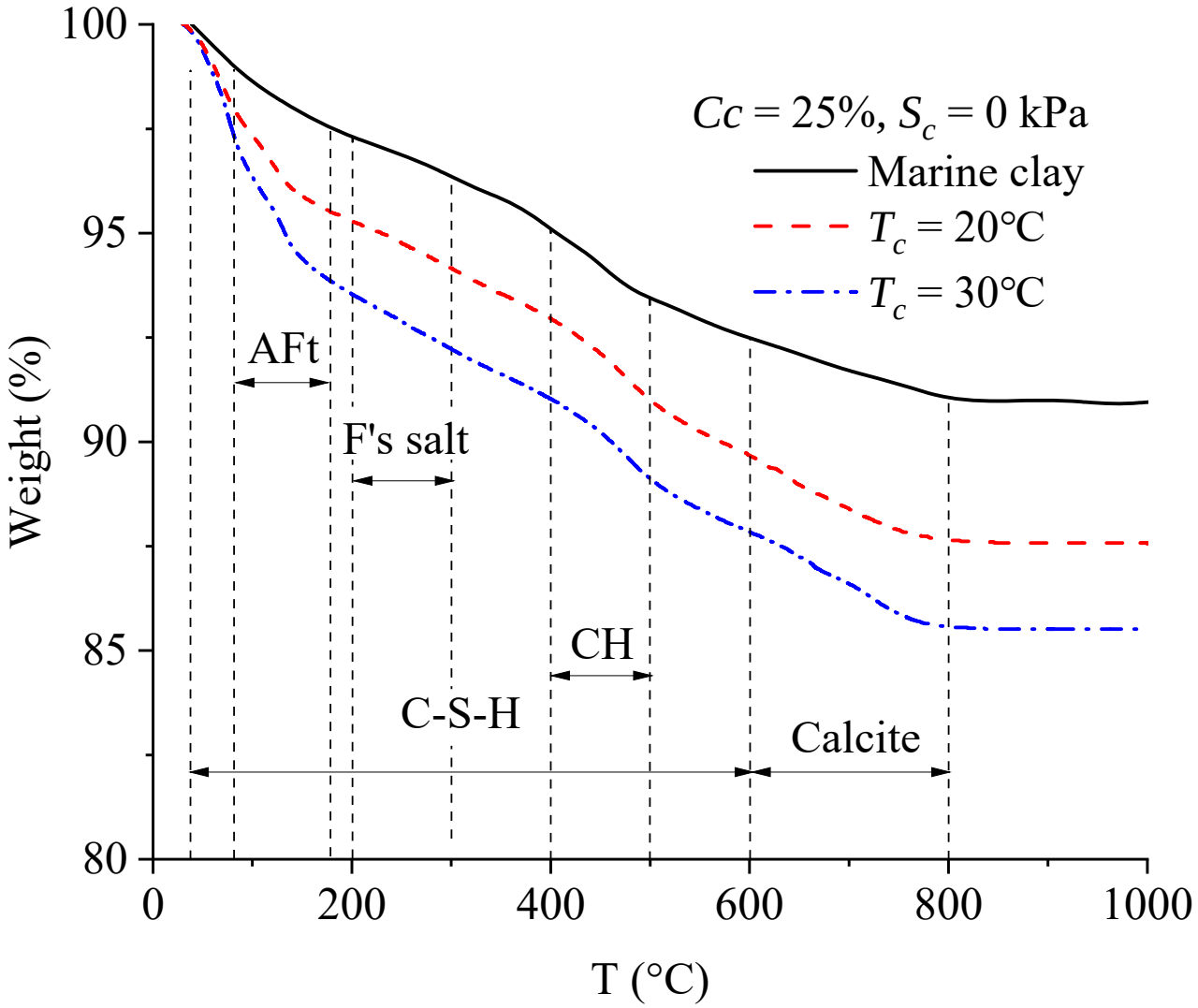

Click here to access/download;Figure;Figure 11b.pdf

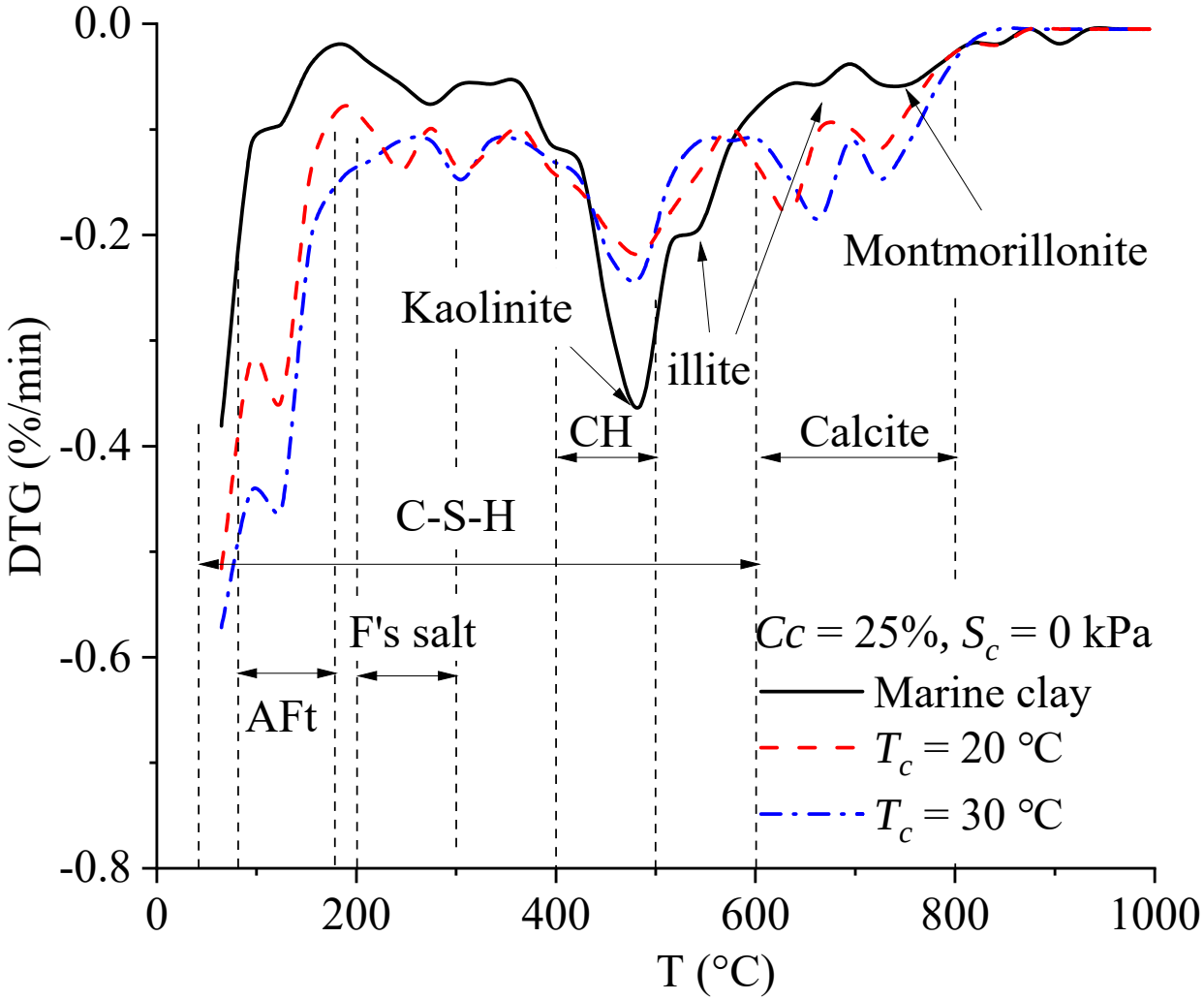

Click here to access/download;Figure;Figure 12.pdf

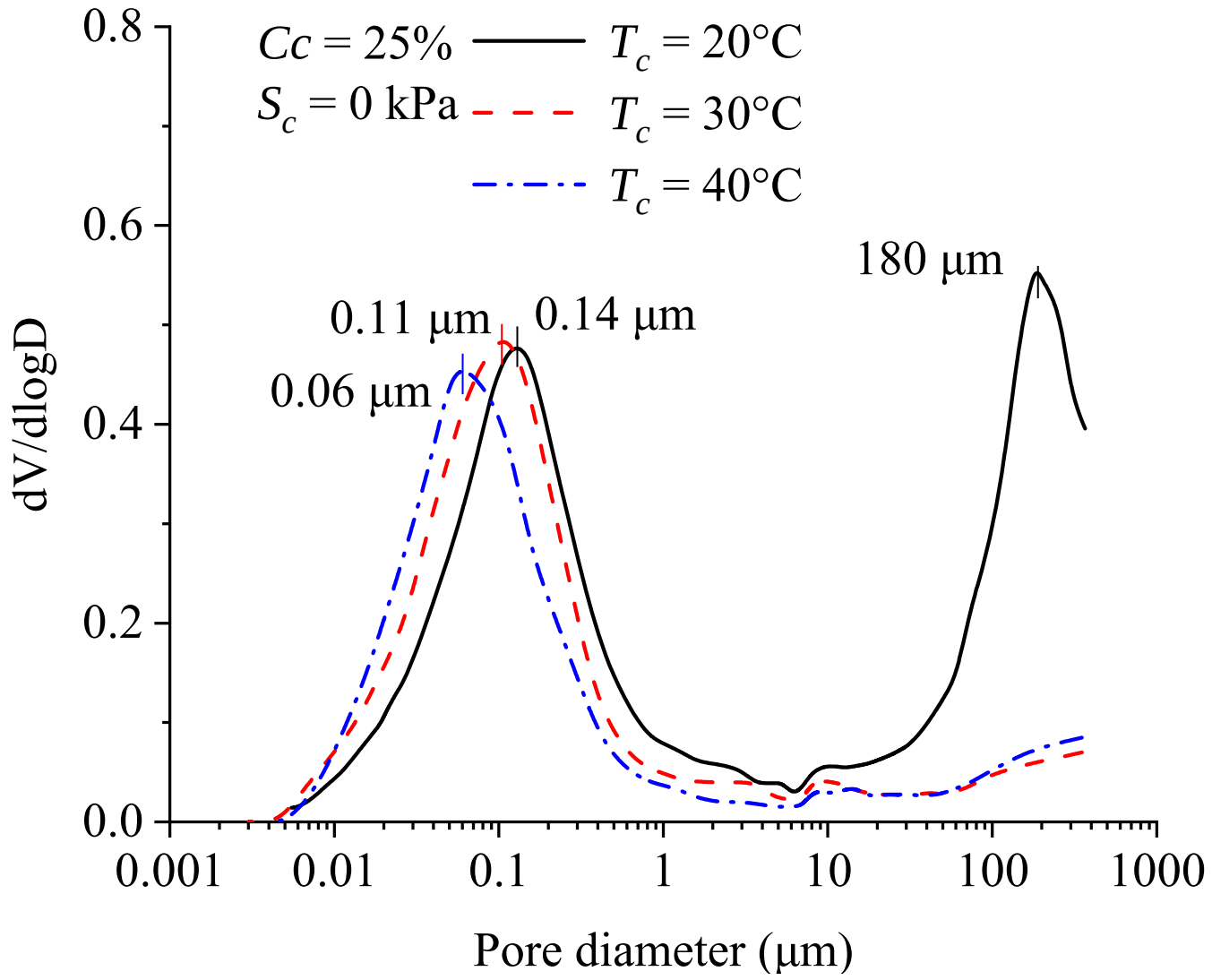

Click here to access/download;Figure;Figure 13a.pdf

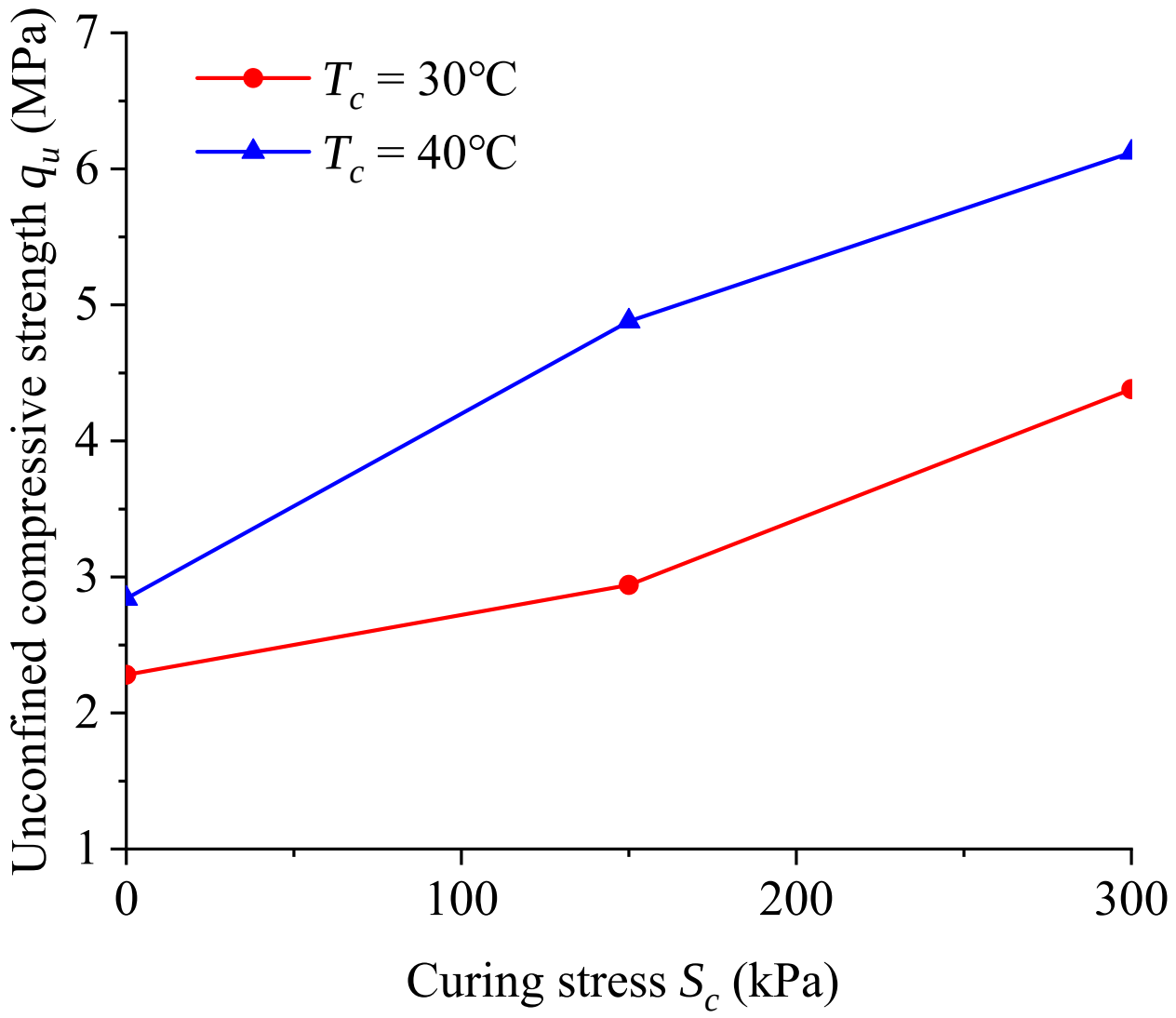

Click here to access/download;Figure;Figure 13b.pdf

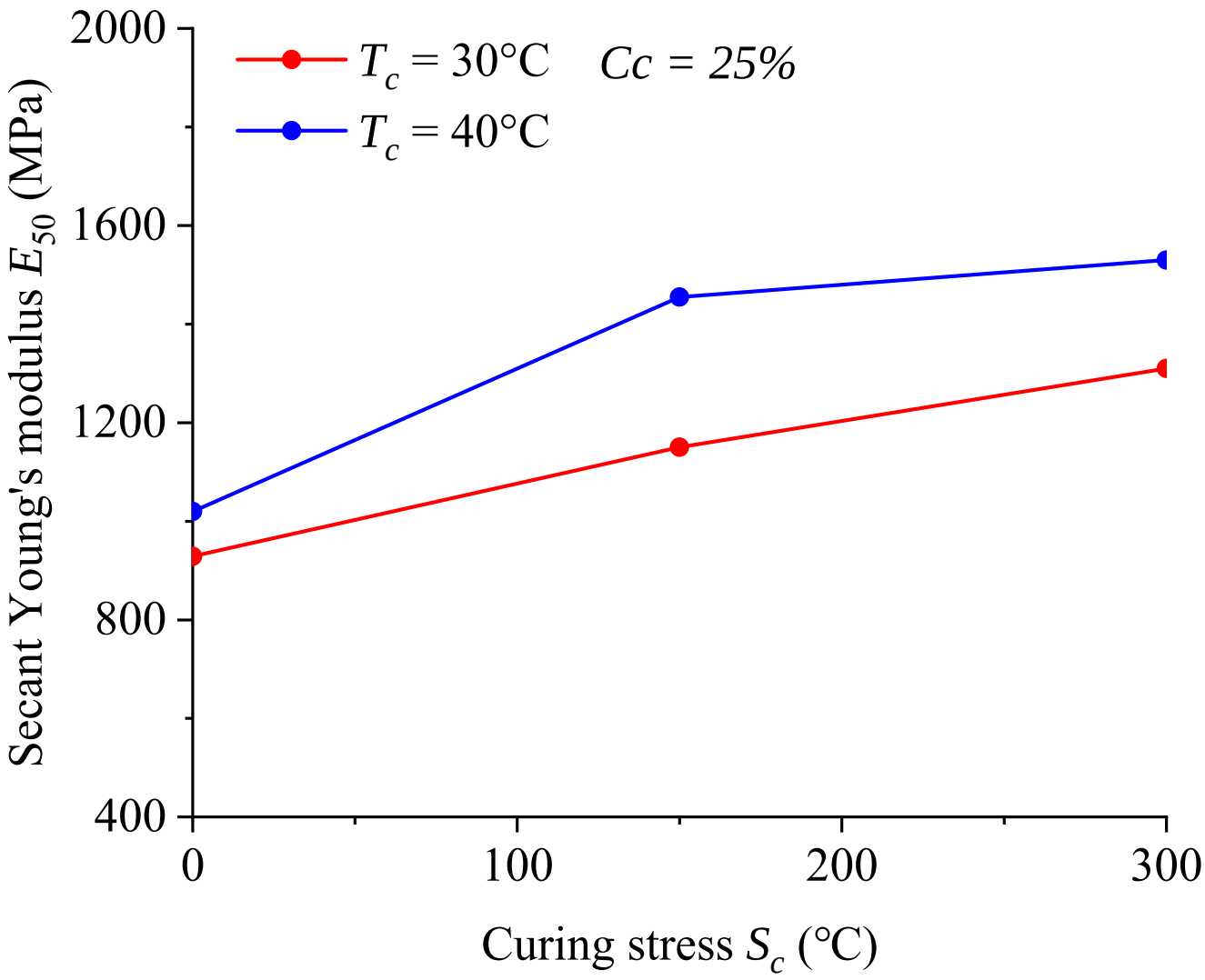

Click here to access/download;Figure;Figure 14a.pdf

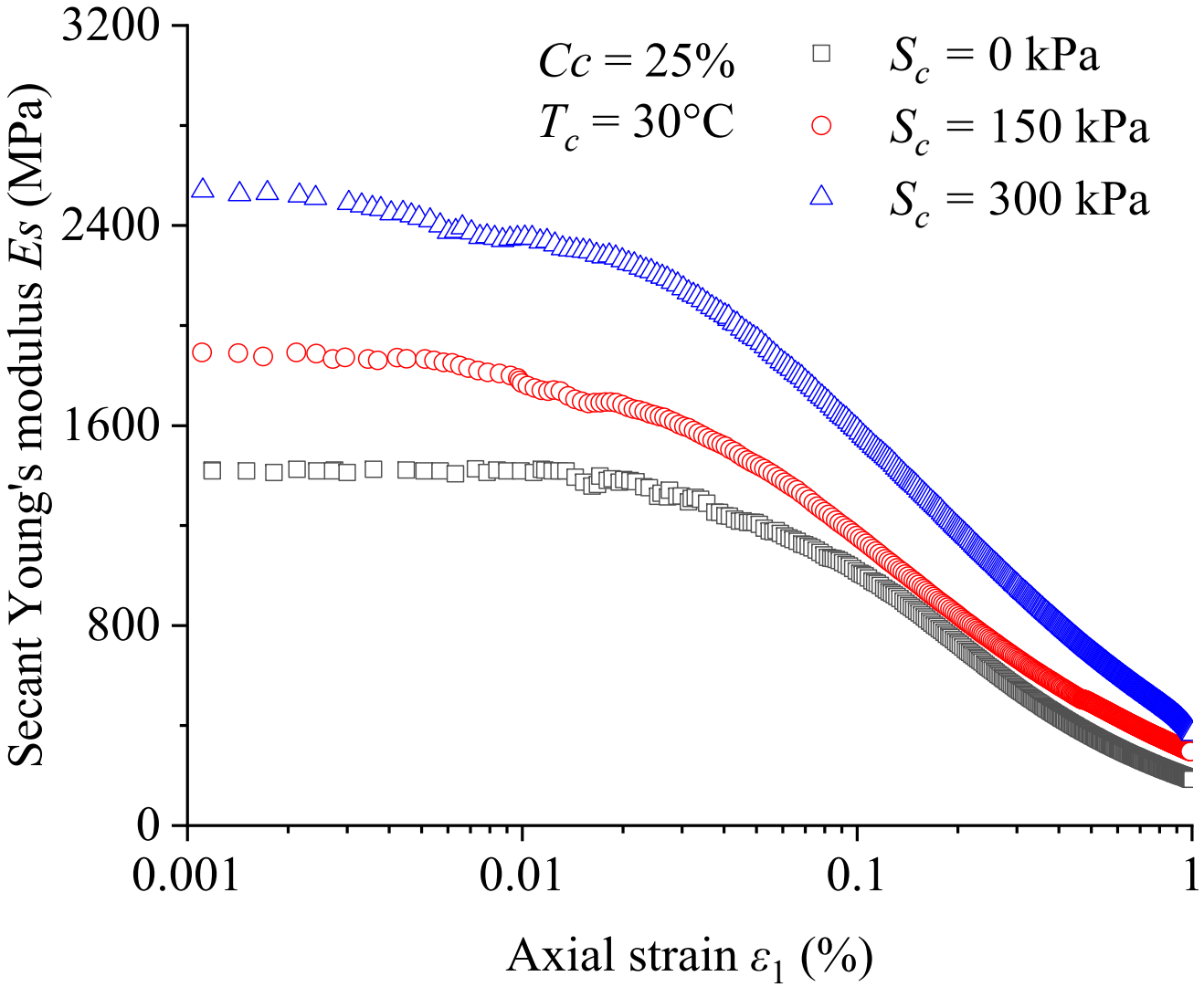

Click here to access/download;Figure;Figure 14b.pdf

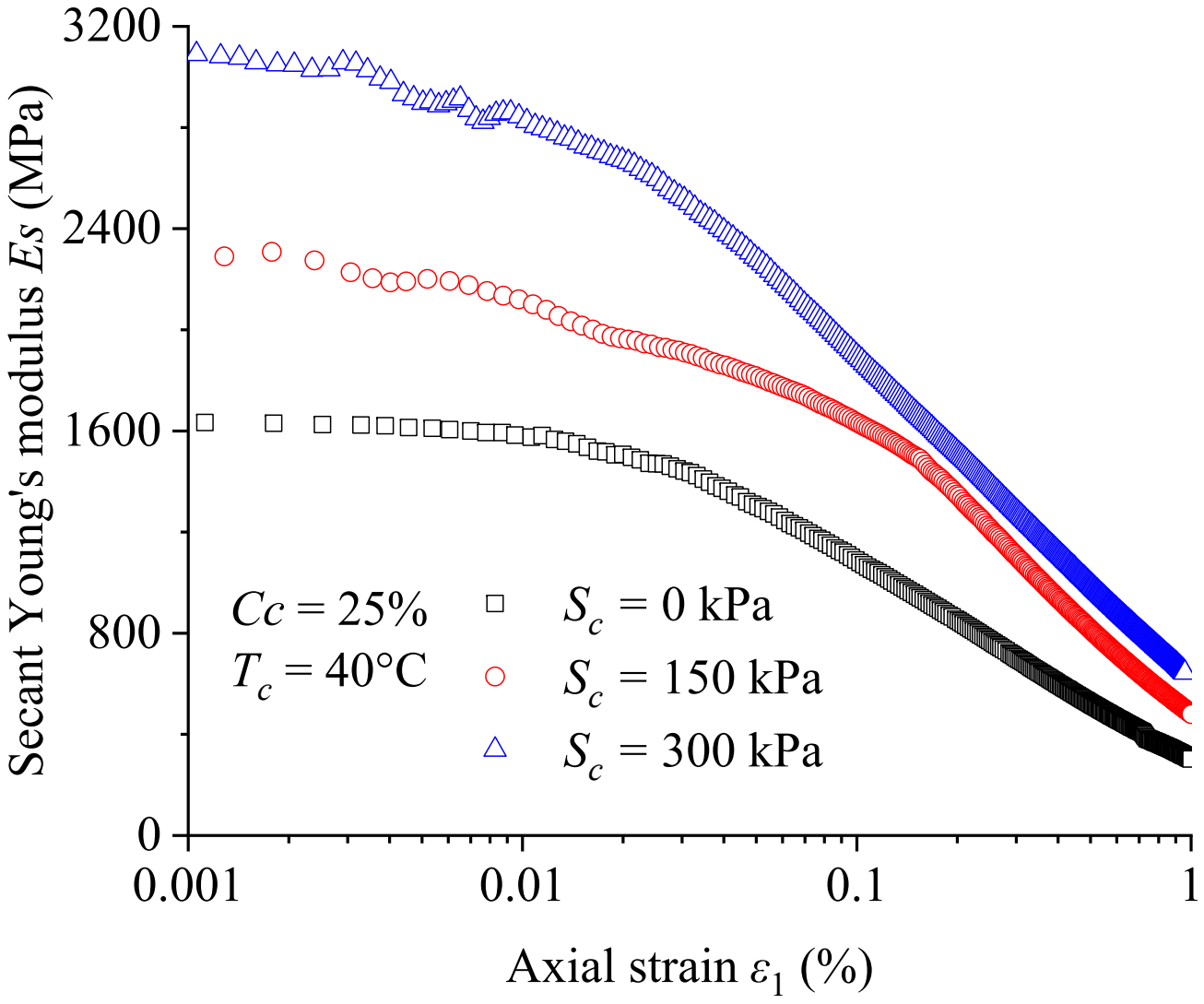

Click here to access/download;Figure;Figure 15.pdf

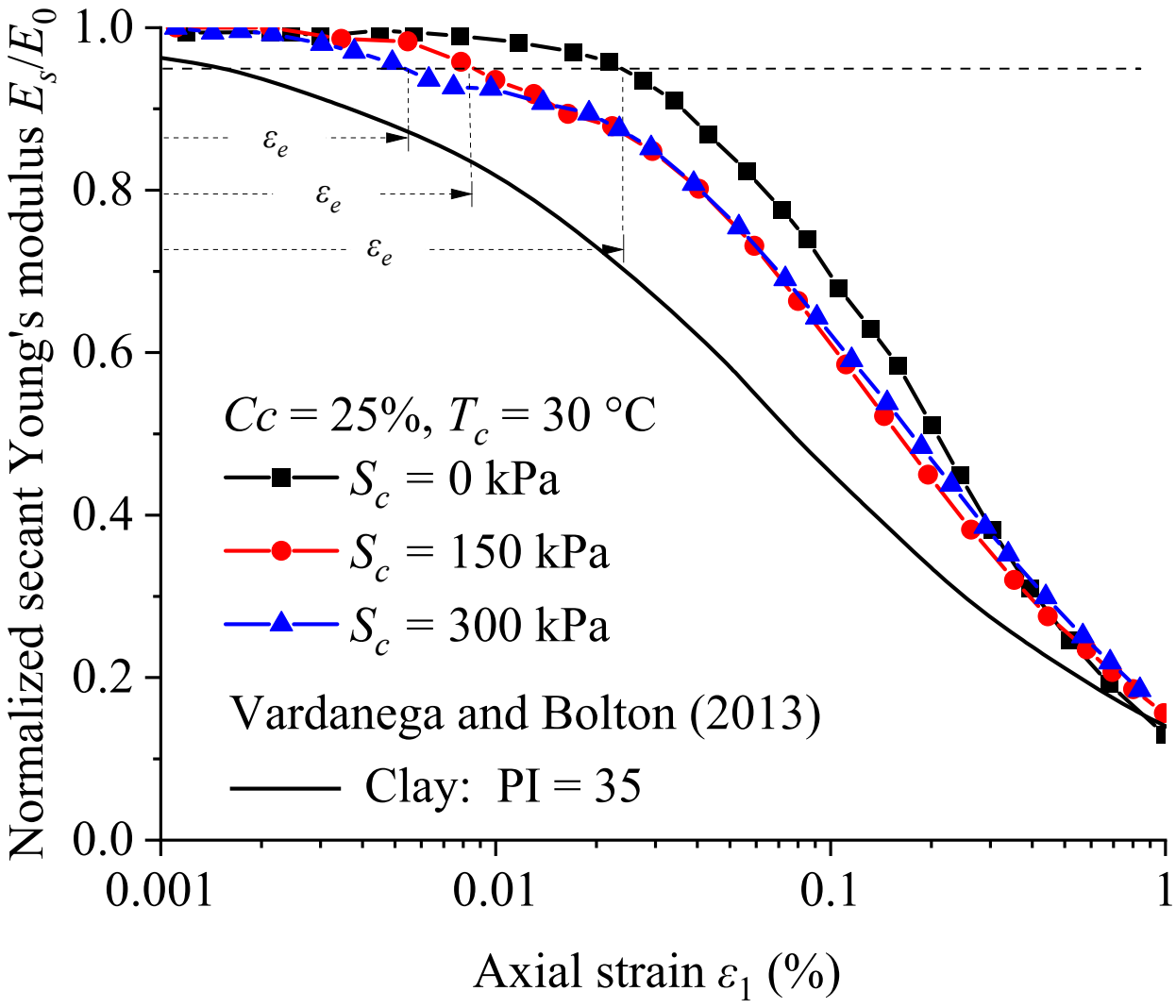

Click here to access/download;Figure;Figure 16a.pdf

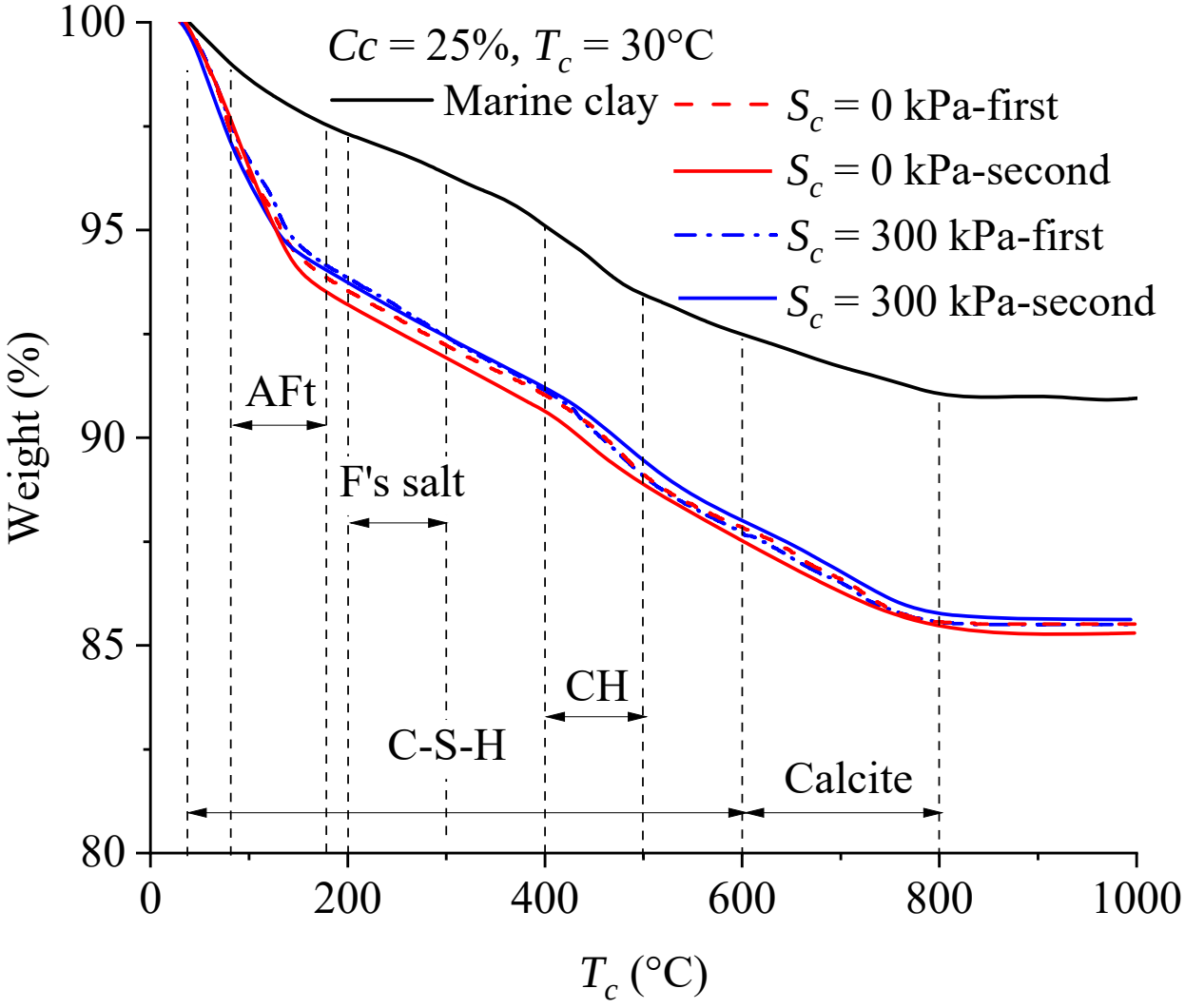

Click here to access/download;Figure;Figure 16b.pdf

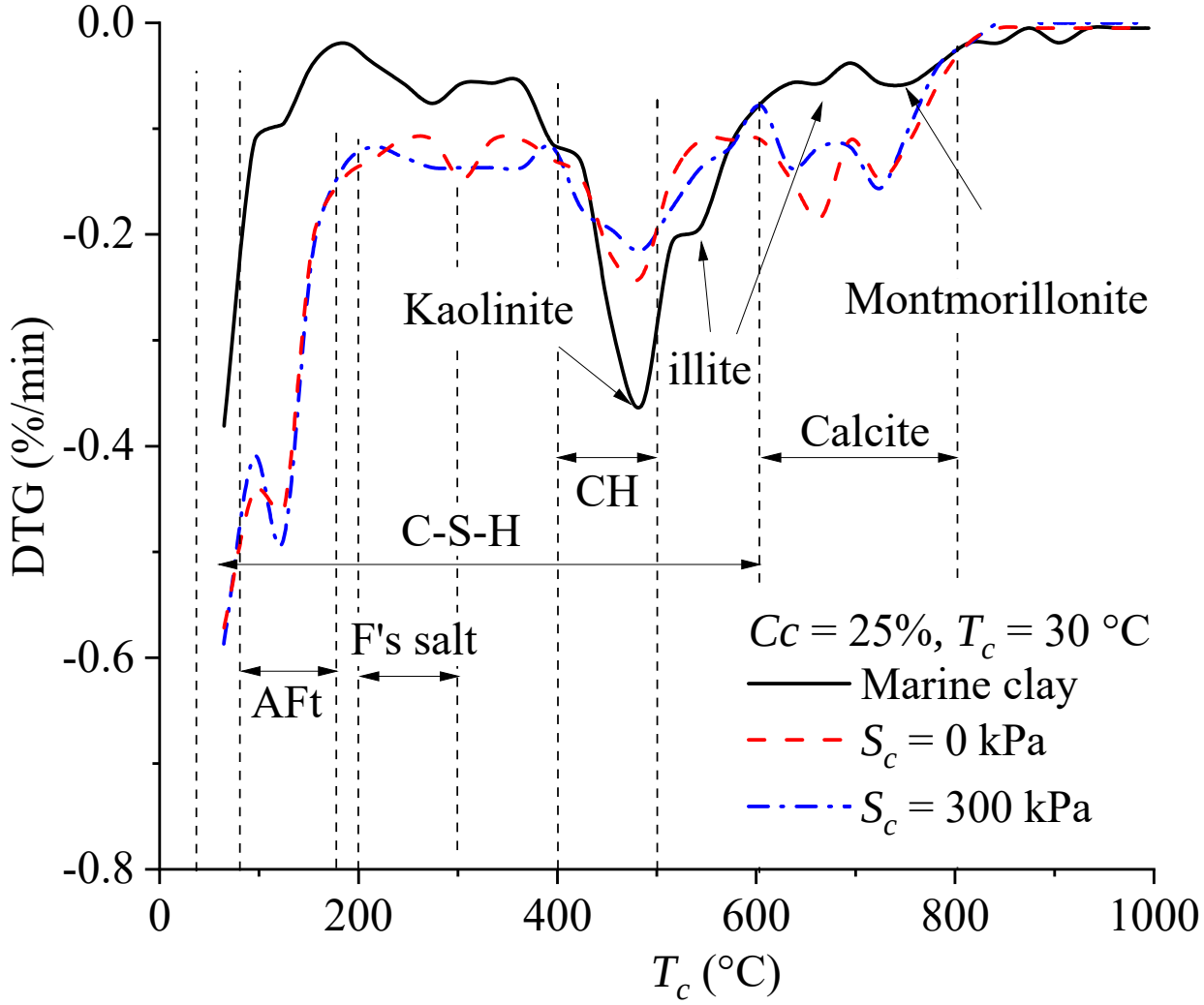

Click here to access/download;Figure;Figure 17.pdf

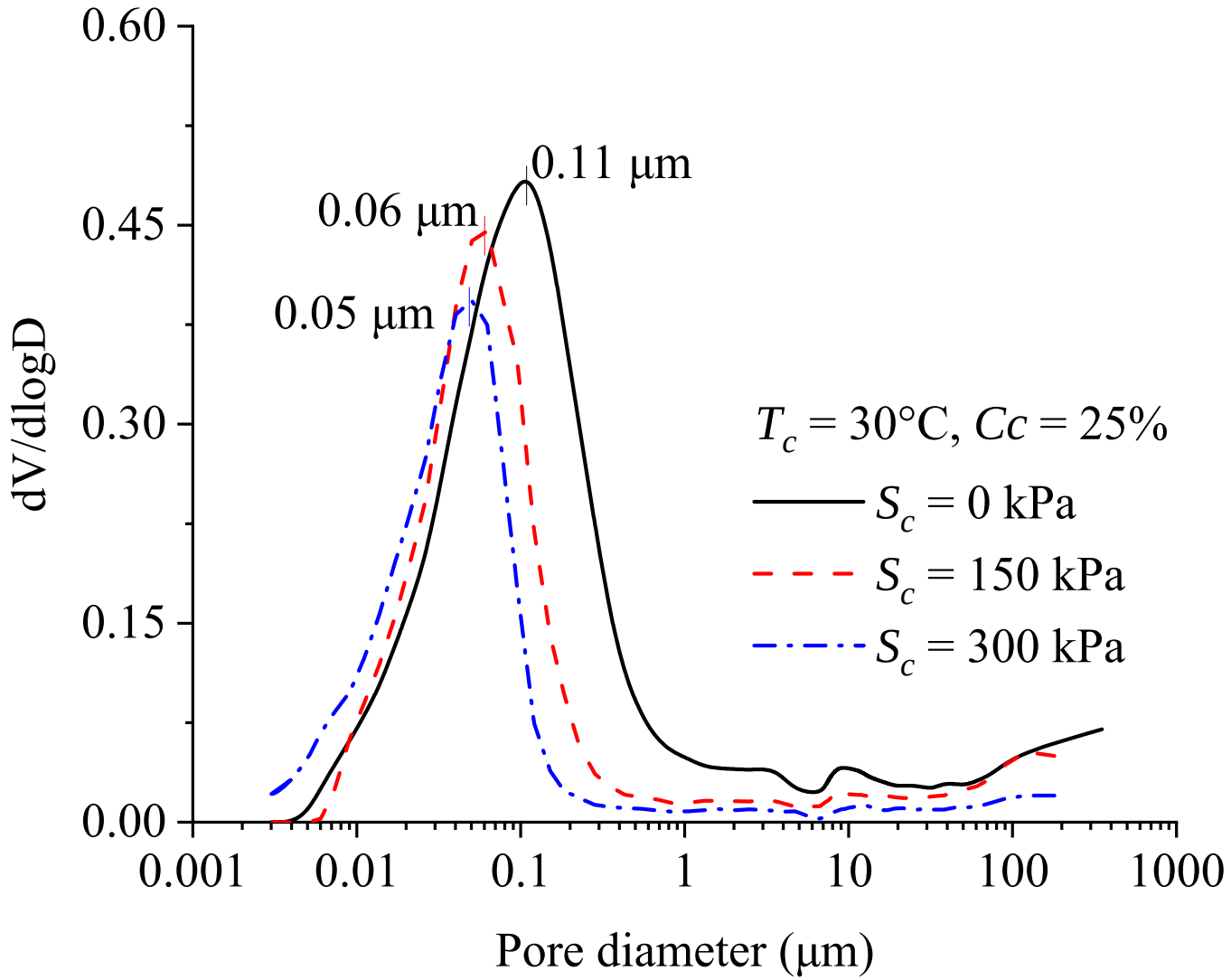

Click here to access/download;Figure;Figure 18a.pdf

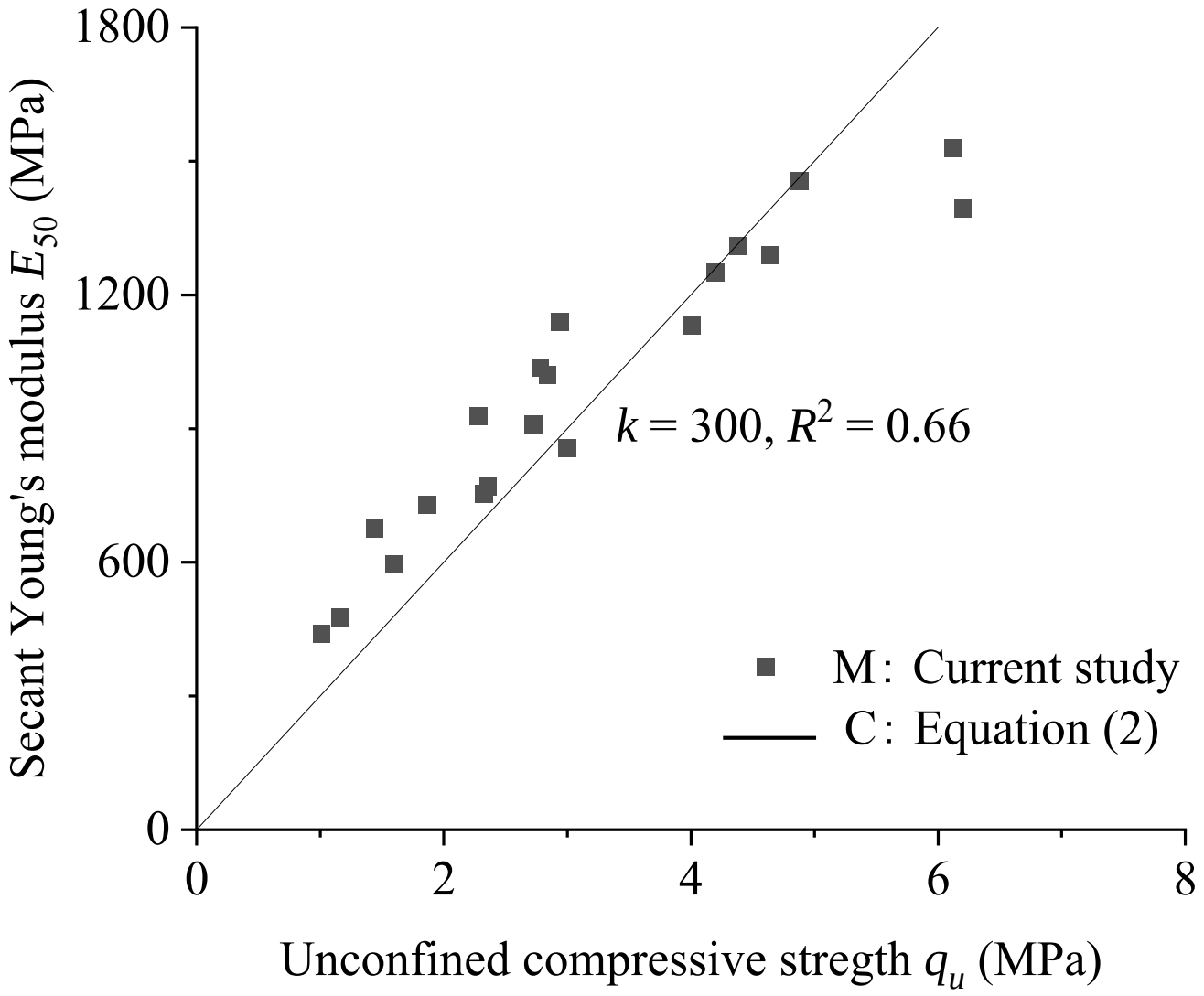

Click here to access/download;Figure;Figure 18b.pdf

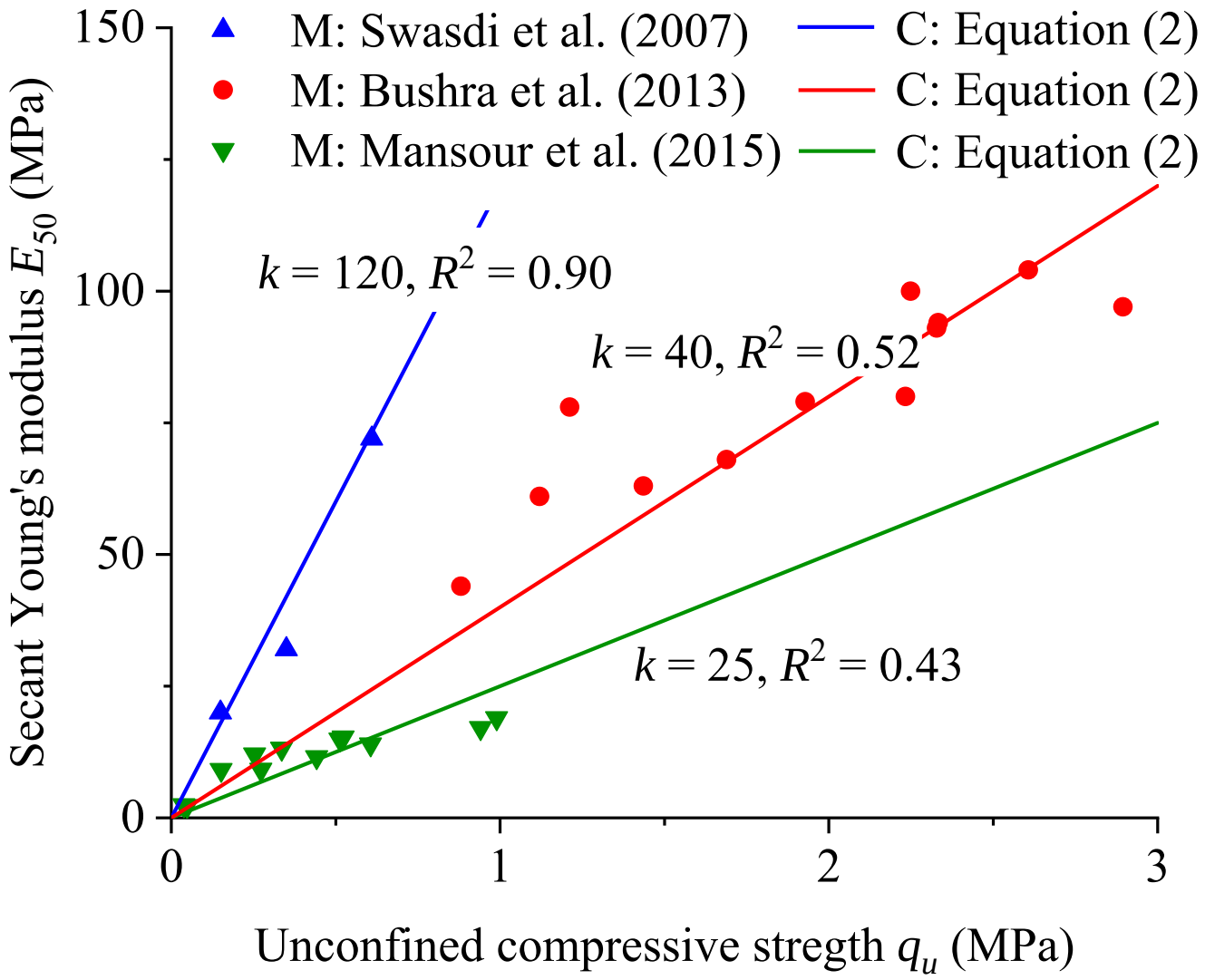

(a) (b)

Click here to access/download;Figure;Figure 18c.pdf

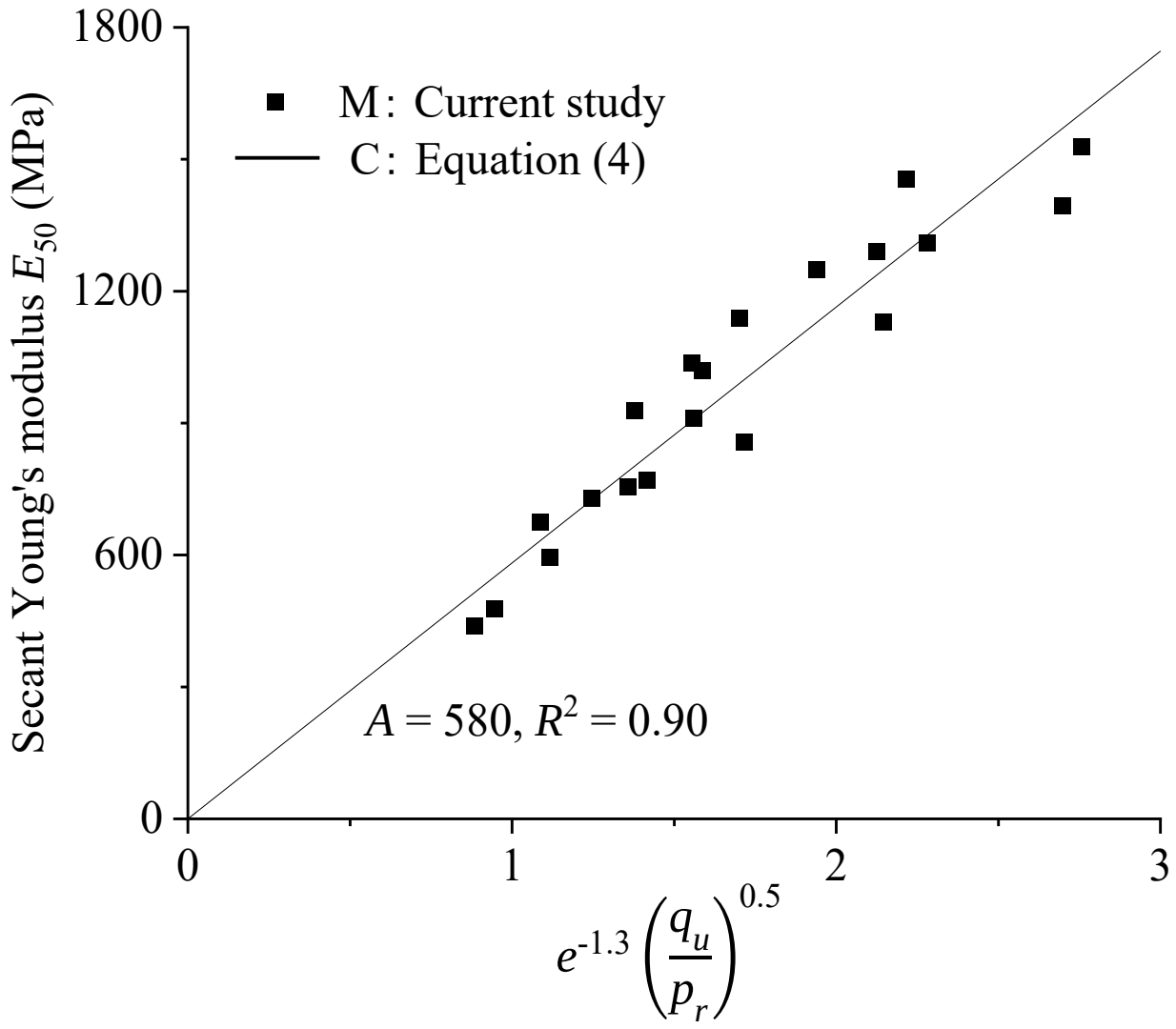

Click here to access/download;Figure;Figure 18d.pdf